Motion Planning of Robotic Systems in Diagnostic and Therapy Applications Using Control and AI

by

Mojtaba Akbari

A thesis submitted in partial fulfillment of the requirements for the degree of

Master of Science

in

Biomedical Engineering

Department of Electrical and Computer Engineering

University of Alberta

Abstract

This thesis presents research on the motion planning of robotic systems in diagnostic and therapy applications, emphasizing the integration of control and AI techniques. Three main contributions are discussed: a robotic ultrasound imaging method, a robot-assisted ultrasound scanning system, and a novel framework for uncertainty-aware control in medical robots.

The first part of the thesis introduces a robotic ultrasound imaging method. This method utilizes a robotic system with five Degrees of Freedom (DoFs) to achieve precise scanning of the breast for high-quality ultrasound images. In the pre-scan phase, the system employs geometrical analysis of the target inside the breast to determine the desired trajectory. In the post-scan phase, the probe's rotational and translational movements are updated based on the center of mass of segmented targets in each acquired frame and the average of the image confidence map. Experimental testing of the proposed visual servoing algorithm on a plastisol phantom demonstrates the system's successful control of the ultrasound probe to target tissue and the algorithm's efficiency in real-time robotic control loops.

The second contribution of this thesis is a robot-assisted ultrasound scanning system designed as a response to the COVID-19 pandemic. During traditional ultrasound scans, the sonographer is in close contact with the patient, increasing the risk of COVID-19 transmission. The proposed system addresses this issue by automating tissue scanning with a dexterous robot arm holding the ultrasound probe. The system continuously assesses the quality of ac-

quired ultrasound images in real-time using a quality assessment algorithm based on correlation, compression, and noise characteristics. The ultrasound image feedback guides the system to automatically adjust the probe contact force, ensuring high image quality. To accomplish this, an SVM classifier is used to analyze the image features and provide feedback to the robot arm for adjusting the scanning force. Experimental testing on plastisol phantom tissue confirms the system's ability to maintain image quality while minimizing the need for direct sonographer-patient contact.

The third contribution of this thesis centers around addressing safety concerns and uncertainty analysis in deep learning-based medical robotic applications for motion planning. Incorporating deep learning algorithms in medical robots introduces uncertainties in real-world scenarios, which can compromise the safety of both the patients and the overall operation. To tackle this challenge, a novel framework for uncertainty-aware control of medical robots is proposed. The study focuses on a lower-limb exoskeleton designed to assist people with disabilities. The framework leverages fast uncertainty analysis to be used in the control loop of the medical robot. By quantifying uncertainty levels during both training and testing phases, the proposed framework ensures safe and reliable human-robot interactions. To achieve this, the framework employs Kullback-Leibler (KL) divergence during the training phase to identify similarities between labels and predictions, while in the test phase, it utilizes Mahalanobis distance to detect out-of-distribution (OOD) data, enhancing safety and improving decision-making for the robot controller. The experiments conducted on the ExoH3 lower-limb exoskeleton demonstrate the effectiveness of the proposed uncertainty analysis technique in real-time motion planning and its capability to detect OOD features that may lead to unsafe motion execution.

Overall, this thesis contributes to advancements in motion planning for

robotic systems in diagnostic and therapy applications, addressing key challenges related to safety and uncertainty. The proposed approaches for robotic ultrasound imaging, robot-assisted ultrasound scanning, and uncertainty-aware control hold the potential for enhancing medical robotics' efficacy and safety, thereby benefiting patients and healthcare providers alike.

Preface

The main contribution of this thesis is the development of innovative approaches in motion planning for robotic systems in diagnostic and therapy applications and addressing safety and uncertainty concerns. This thesis is part of a multidisciplinary research collaboration, led by Dr. Mahdi Tavakoli (principal investigator) at the Department of Electrical and Computer Engineering, University of Alberta, and Dr. Lei Ma at the Department of Electrical and Computer Engineering, University of Alberta. All of the work presented in this thesis was conducted in the Telerobotic and Biorobotic Systems Lab at the University of Alberta.

I was responsible for the experiment design, performing the experiments, data collection and analysis, and manuscript preparation. Also, the experimental setup was designed by myself. Dr. Mahdi Tavakoli was the supervisory author on this project and was involved throughout the project in concept formation and manuscript composition.

Chapter 1 presents the motivation and objectives of this project and summarized the thesis organization and contributions. Chapter 2 reviews state-of-the-art motion planning algorithms related to this research project.

Chapter 3 of this thesis has been presented as: Mojtaba Akbari, Jay Carriere, Ron Sloboda, Tyler Meyer, Nawaid Usmani, Siraj Husain, Mahdi Tavakoli, "Robot-assisted Breast Ultrasound Scanning Using Geometrical Analysis of the Seroma and Image Segmentation," 2021 IEEE/RSJ International Conference on Intelligent Robots and Systems (IROS), Prague, Czech Republic, 2021, pp. 3784-3791, doi: 10.1109/IROS51168.2021.9636401.

Chapter 4 of this thesis has been published as: Akbari, Mojtaba, Jay Carriere, Tyler Meyer, Ron Sloboda, Siraj Husain, Nawaid Usmani, and Mahdi

Tavakoli. "Robotic ultrasound scanning with real-time image-based force adjustment: quick response for enabling physical distancing during the COVID-19 pandemic." Frontiers in Robotics and AI 8 (2021): 645424.

Chapter 5 of this thesis has been submitted as Mojtaba Akbari, Javad K. Mehr, Lei Ma, Mahdi Tavakoli, "Uncertainty-aware Safe Adaptable Motion Planning of Lower-limb Exoskeletons Using Random Forest Regression," Mechatronics, 2023

This thesis is dedicated to my beautiful wife, Marjan and my supportive parents

Acknowledgements

This MSc thesis would not have been possible without the guidance, support and help of my supervisors, family, and friends. First and foremost, I would like to thank my supervisor, Dr. Mahdi Tavakoli, who believed in my abilities and supported and encouraged me to push my limits past what I initially thought was possible. I am incredibly thankful and consider myself truly lucky to have worked with a successful, incredibly patient, caring, and outstanding mentor and role model. He has made it possible for me to enjoy access to a world-class lab facility and the most advanced robots. I would like to thank my co-supervisor, Dr. Lei Ma, for his insightful comments and feedback, and for his expert advice and suggestions.

Many thanks to the current and past members of the Telerobotic and Biorobotics Lab at the University of Alberta. Thanks to Javad K. Mehr, Amir Zakerimanesh, Mehrnoosh Afshar, Abed Soleymani, Paniz Sedighi, Teng Li, Yafei Ou, Yi Hu, Kirill Makhachev, Mojtaba Akbari, Teng Li, Javad Khodaei-Mehr, Amir Zakerimanesh, Abed Soleymani, Jay Carriere, Ali Torabiparizi, Mojtaba Sharifi, Mahdi Abdollah Chalaki, Amir Abdolmaleki, Sadra Zargarzadeh, Mahdi Fazeli, Masoud Jafaripour, Yeganeh Aliyari Shooredeli, and Hongjun Xing for the help, advice, discussions, support, and friendship.

Most importantly, I must wholeheartedly extend my deepest appreciation to my dearest and enchanting wife, Marjan. Her boundless love, unwavering support, and selfless sacrifices have been the driving force behind the completion of this thesis. She has forever been the cherished love of my life, providing invaluable insights, profound understanding, and unwavering encouragement throughout this journey.

Finally, I would like to thank my parents, parents-in-law, little sister and

her husband, and sister-in-law for their constant love, encouragement, understanding, patience, and support. I am indebted to each of you.

This research was supported by the Canada Foundation for Innovation (CFI), UAlberta Huawei-ECE Research Initiative (HERI), the Government of Alberta, the Natural Sciences and Engineering Research Council (NSERC) of Canada, the Canadian Institutes of Health Research (CIHR), and the Alberta Economic Development, Trade and Tourism Ministry's grant to Centre for Autonomous Systems in Strengthening Future Communities.

Contents

List of Tables

List of Figures

Chapter 1

Introduction

1.1 Motivations

In recent years, the integration of robotic systems into diagnostic and therapy applications has shown the potential in revolutionizing healthcare practices. These robotic systems possess the ability to enhance precision, efficiency, and patient outcomes. Among the critical aspects of implementing such robotic systems lies the concept of motion planning, which plays a pivotal role in ensuring safe, accurate, and optimal movements of robotic devices during medical procedures.

The primary motivation behind this thesis titled "Motion Planning of Robotic Systems in Diagnostic and Therapy Applications Using Control and AI" stems from the need to address the complexities and challenges associated with motion planning in medical robotics. As medical procedures continue to evolve with cutting-edge technologies, the demand for sophisticated, adaptable, and autonomous robotic systems becomes increasingly evident.

The thesis seeks to delve into the intricacies of motion planning in diagnostic and therapy applications, emphasizing the significance of incorporating both control techniques and artificial intelligence (AI) algorithms. The fusion of control and AI empowers robotic systems with the ability to navigate complex environments, dynamically adjust movements, and respond intelligently to unexpected scenarios, thereby ensuring patient safety throughout medical interventions.

The thesis focuses on two specific applications that hold great promise in

the realm of medical robotics. The first application involves ultrasound breast scanning for surgery. By employing advanced motion planning techniques, the thesis aims to optimize the scanning process, allowing for precise imaging of breast tissues and facilitating more accurate diagnostic and surgical procedures.

The second application considered in this thesis pertains to exoskeletons for rehabilitation purposes. By incorporating sophisticated motion planning strategies, the thesis seeks to enhance the control and coordination of lower-limb exoskeletons, assisting people with disabilities in their rehabilitation journey. Through robust motion planning, these exoskeletons can better adapt to user movements, provide a more natural gait, and ensure the safety and comfort of patients during rehabilitation sessions.

With a primary focus on two fundamental applications in medical robotics, namely surgery and rehabilitation, this thesis places safety at the forefront of its endeavours. The envisioned outcomes have the power to drive medical robotics toward an era of heightened precision, efficiency, and patient-centred care. By pushing the boundaries of motion planning techniques, and leveraging the integration of control and AI, this research aims to make a contribution to the dynamic landscape of medical technology. Ultimately, the objective is to elevate patient outcomes.

1.1.1 Ultrasund Image-based Surgical Motion Planning

The field of medical robotics has witnessed significant advancements, offering promising applications in various domains of healthcare. Among these applications, two critical areas of interest are surgery and rehabilitation. Robotic systems have demonstrated their potential to enhance surgical precision and aid in rehabilitation processes, revolutionizing patient care. However, successful integration of medical robotics relies heavily on motion planning algorithms that ensure safe and accurate movements of robotic devices, particularly in ultrasound image-based surgical procedures.

Ultrasound (US) imaging has emerged as a widely used and safe medical imaging modality, offering a low-cost alternative to modalities like MRI,

CT, and X-ray. Despite the inherent challenges of low signal-to-noise ratios in US images, leveraging robotic systems to hold the US probe during scanning presents an opportunity to address factors affecting image quality, such as probe orientation and tissue contact force. In this context, robot-assisted US scanning has garnered attention due to its potential to generate high-quality images autonomously or in collaboration with sonographers. Enhancing motion planning techniques in robot-assisted US scanning holds the promise of optimizing imaging processes, ensuring better visualization of anatomical structures, and facilitating accurate interventions during surgical procedures.

Breast cancer diagnosis and treatment represent a prominent application of US image-based surgical motion planning. Breast conservation surgery, such as lumpectomy, followed by brachytherapy, has gained popularity for its cosmetic advantages. To ensure precise needle insertion during radiation therapy, accurate segmentation of the seroma (a fluid-filled area post-lumpectomy) in US images is crucial. The proposed fully-autonomous US image scanning algorithm seeks to precisely control the US probe's position and orientation based on a pre-scan phase for seroma analysis and a post-scan phase for optimal visualization. The ability to repeatedly scan the seroma autonomously holds promise for further required steps, such as 3D reconstruction of the breast.

The assessment of image quality plays a vital role in developing effective robotic US scanning systems. Quality metrics become especially challenging in US images due to inherent noise, impacting a physician's interpretation. In this context, no-reference image quality assessment algorithms are critical in the absence of quality reference images. This thesis proposes a novel method for US image quality assessment in the presence of a robotic arm holding the US probe. Integrating the proposed algorithm into the robot control loop enables automatic tissue scanning with the assistance of an admittance-based controller. The robotic assistant, equipped with the ability to analyze image quality, adjusts the US scanning force applied to the tissue autonomously, reducing contact time between the sonographer and the patient, thus mitigating the risk of virus transmission. The proposed system optimizes scanning efficiency and enhances patient safety by employing image quality assessment

feedback for autonomous scanning, allowing the sonographer to focus on critical aspects of the procedure.

1.1.2 Post-diability Gait Rehabilitation Motion Planning

Deep learning has shown tremendous promise in various medical applications, fueled by the abundance of available data and the data-driven system development approach. However, in safety-critical domains such as medical robotics, concerns about the quality and reliability of deep learning-based methods persist. The integration of data-driven Artificial Intelligence (AI) as decision-makers in medical robots demands thorough safety analysis, particularly given the potential consequences of uncertain predictions. Deep learning models lack statistical guarantees for handling scenarios beyond their training distribution, making it essential to address uncertainties in their decision-making processes. In the context of medical robots, where AI-driven systems rely on imagers and sensors to make critical decisions, the need for robust uncertainty assessment becomes even more critical to ensure safety in human-robot interaction.

This thesis seeks to address the challenge of incorporating the uncertainty of deep learning decision-makers into the control loop of medical robots while maintaining real-time efficiency. Notably, we propose a novel approach to employ random forest regression (RFR) to predict the passive dynamics of the human-exoskeleton system, using joint positions, velocities, and accelerations as inputs. By estimating human-exoskeleton interaction torques, we inform and update motion planning, enhancing the safety of human-robot interaction. Our contribution lies in integrating uncertainty estimation into the Central Pattern Generator (CPG) dynamics for gait motion planning, effectively reducing potential safety risks. Leveraging Kullback-Leibler (KL) divergence and Mahalanobis distance, we develop a comprehensive uncertainty analysis technique that measures RFR uncertainty and detects out-of-distribution data points. This framework ensures adaptability to different learning techniques, offering a robust safety-enhancing solution for AI-powered medical robots in post-disability gait rehabilitation motion planning.

1.2 Dissertation Contributions and Overview

The major contributions of this dissertation are summarized as follows:

- **Ultrasound Image-based Surgical Motion Planning:**
  - We propose a visual servoing algorithm that controls five Degrees of Freedom (DoFs) of the probe during breast scanning. The algorithm employs a two-phase approach, pre-scan and post-scan, to analyze geometrical features of the seroma and ensure visualization during US imaging.
  - The integration of image feedback and admittance control in the US scanning procedure represents a novel approach. This allows for effective collaboration between humans and the robotic system, enhancing safety during medical procedures.
  - We introduce a real-time image quality assessment algorithm to inform the robotic system, facilitating clinician-in-the-loop robot-assisted medical applications. The combination of admittance control and online image quality assessment ensures social distancing during the COVID-19 pandemic, presenting an unexplored solution in the literature.
- **Context of COVID-19 Pandemic and Medical Robotics:**
  - We propose a rapid, cost-effective, and deployable solution to address COVID-19 concerns during US scanning. The system can be trained based on sonographers' preferences for different applications, providing the flexibility to tailor the system to specific needs.
  - Our proposed method can be used in unilateral tele-sonography as a local controller on the patient side, removing the need for haptic feedback and reducing system costs. The system adjusts the force applied to the tissue based on acquired image quality, ensuring safe and efficient remote US scanning.

- **Uncertainty Analysis for Deep Learning-based Medical Systems:**
  - We introduce a novel uncertainty analysis technique that considers both training and testing data distributions. Leveraging KL divergence and Mahalanobis distance, we provide a reliable prediction uncertainty measure for deep learning-based medical systems.
  - Our proposed uncertainty technique enhances the safety of human-robot interaction during task execution by detecting potentially unsafe actions of the exoskeleton resulting from less certain predictions.
  - We leverage Random Forest Regression (RFR) to predict the interaction torque between the exoskeleton and the passive component of human-exoskeleton dynamics. RFR's model-free nature and low computational complexity make it a suitable choice for real-time control requirements compared to traditional methods.

Through these contributions, this thesis advances the field of Ultrasound Image-based Surgical Motion Planning, addresses COVID-19 safety concerns in medical robotics, and introduces a novel uncertainty analysis technique for deep learning-based medical systems, fostering improved precision, efficiency, and safety in medical applications.

This thesis is structured as follows: Chapter 2 presents a summary of the literature. In Chapter 3, we propose a visual servoing algorithm that controls five DoFs of the probe during the scanning of the breast. The proposed method has two phases called pre-scan and post-scan to analyze the geometrical features of the seroma and design the controller to keep the seroma in the field of view. We present our image quality-based ultrasound scanning algorithm in 4. In Chapter 5, we present our proposed uncertainty-aware safe adaptable motion planning of exoskeleton using the uncertainty of deep learning decision-makers in the control loop of the robot. The proposed method in 5 maintains the real-time necessity of the algorithm to be used in the controller

of the robot. We conclude and discuss future work in Chapter 6.

Chapter 2

Literature Review

2.1 Motion Planning for Ultrasound Breast Scanning

Robots have proven to be valuable assistants for sonographers during US scanning. For instance, in [43], authors develop a 4-DoF robotic wrist to perform liver and kidney US imaging, where a teleoperated wrist obtains US images with the robot maintaining US scanning force on the patient's body. In [15], a cooperative robotic US system is proposed, consisting of a 6-DoF robotic arm holding the US probe and a dual force sensor setup enabling cooperative control and adaptive force assistance using admittance force control. Authors in [61] introduce an impedance-controlled teleoperation system for robot-assisted tele-echography of moving organs, compensating for organ motions using two impedance models for local and remote robots. Additionally, [54] presents a solution for energy management in tele-echography, and [4] reviews various methods in robot-assisted US intervention. However, these methods commonly utilize two robots, imposing additional costs and challenges like communication delays and haptic feedback requirements for the local robot. To address these concerns, our thesis proposes an autonomous system for scanning that eliminates the need for local and remote robots.

The implementation of US visual servoing involves relating the position, velocity, and/or force control of the US probe to features seen in the US image using various transformations like shearlet, wavelet, DCT, PCA, and confidence maps. For instance, [14] utilizes the shearlet transform and links

shearlet decomposition coefficients to the US probe's velocity during scanning. Similarly, [48] controls six DoFs of the robot using the wavelet transformation, and [37] proposes visual servoing based on PCA algorithm projection. While these methods demonstrate effectiveness, our thesis introduces a novel method that utilizes US images in both pre-scan and post-scan phases, reducing costs and ensuring safer operations.

Preprocessing methods like confidence maps have also been employed for US image-based visual servoing. For instance, [28] introduces the confidence map based on the US signal attenuation inside the tissue. [9] uses a confidence map to control three DoFs of the US scanning robot and investigates the relationship between probe positioning and US image quality. [10] proposes a method based on an image confidence map to track a specific target inside the tissue during scanning. Our thesis is motivated by the need to propose a completely US-based method for scanning, which reduces costs and enhances safety compared to relying on MRI and CT data for pre-scan information. By incorporating US images in both pre-scan and post-scan, our proposed method achieves cost-effectiveness and improved safety for the visual servoing system.

2.2 Image Quality based Motion Planning

2.2.1 Medical Image Quality Assessment

Medical image quality assessment is a complex field encompassing various imaging modalities, each with its unique features and characteristics. A comprehensive review of medical image quality assessment algorithms and corresponding imaging modalities is available in [12]. The lack of reference data poses a critical challenge in medical image quality assessment, leading to the development of no-reference image quality assessment algorithms. These can be classified into model-based and image-based methods. In the former, both images and noise are modeled, as demonstrated in [68], where Noise-Equivalent Quanta (NEQ) is employed to model noise based on US machine parameters and tissue properties.

In the context of US image quality assessment, various methods have been

proposed for modeling image and noise characteristics. For instance, [68] introduces NEQ as an improved signal-to-noise ratio, incorporating US machine parameters and tissue properties for noise modeling. Additionally, the Structural Similarity Index Measure (SSIM) is widely used in image quality assessment, as shown in [52], which utilizes SSIM along with specific image features like preserved edges, structural similarity, and textures.

Image-based quality assessment methods define criteria formalizing essential features for quality evaluation. In [22], quality assessment metrics for US images are formalized using data management and acquisition techniques. Similarly, [3] employs the wavelet transform to extract five important features (sharpness, illumination, homogeneity, field definition, and content) from transformed images, combining them into a quality assessment metric for human retina images.

US imaging presents unique challenges in quality assessment due to the inherent noise in US images. Quality is often defined by the ability to discern tissue features or organs. For instance, [71] proposes a method using the texton approach for segmenting the fetus in US images and uses a random forest classifier to assess image quality based on the extracted features. Similarly, [57] extracts three features from breast US images (nipple position, nipple shadow, and breast contour shape) and employs a random forest for classification. [55] expands on this approach, incorporating 14 features and a correlation matrix for quality assessment. Deep Convolutional Neural Networks (CNN) have also shown promising results in complex tasks like this. [66] utilizes two deep CNNs, C-CNN and L-CNN, where L-CNN identifies the Region Of Interest (ROI) and C-CNN evaluates image quality based on the ROI. The output of C-CNN provides binary label segmentation of the US image. Additionally, [9] and [64] utilize confidence maps proposed in [28] to orient and move the US probe during tissue scanning. Confidence map methods leverage US signal propagation models within the tissue to extract features used as inputs to the controller, generating control signals for the probe's orientation and position.

2.2.2 Robot-assisted Sonography

Robots have proven to be valuable assistants to sonographers during US scanning, and various methods have been proposed to enhance the sonography process using robots. For instance, [43] developed a 4-DoF robotic wrist for remote US imaging, utilized for liver and kidney scanning. Similarly, [1] introduced a robotic mechanism that, when placed on the patient's body, is controlled by a US expert to facilitate the scanning procedure, ensuring consistent contact between the US probe and the patient's body. Additionally, [15] proposed a cooperative robotic US system with a 6-DoF robotic arm that holds and actuates the US probe. The system incorporates a dual force sensor setup, enabling cooperative control and adaptive force assistance through admittance force control. For comprehensive reviews of robot-assisted US interventions and mechanical aspects of robot-assisted US scanning, [4] and [41] are valuable sources, respectively.

Tele-sonography systems have been developed for scanning tissues using remote robots. [61] presented an impedance-controlled teleoperation system for robot-assisted tele-echography of moving organs such as the heart, chest, and breast. This system utilizes two impedance models for master and slave robots, allowing the slave robot to follow the master robot's trajectory while complying with the oscillatory interaction forces of moving organs, providing feedback to the sonographer. Addressing energy consumption challenges in tele-echography on the master site, [54] proposed a solution involving proper scaling of the energy exchanged between the master and slave sites. Despite the advantages of tele-sonography, challenges exist, including high system costs and the need for haptic feedback in the master site, leading to potential time delays between the sonographer and US probe during scanning. Our proposed method can serve as a local controller in the slave site, mitigating such challenges and ensuring effective tele-sonography procedures.

2.2.3 Robot Admittance Control

The admittance controller relies on a predetermined relationship between force and position, and its application has been explored in various contexts. In the field of co-manipulated US scanning systems, [8] employed admittance control to ensure compliance, regulating the force applied to the tissue and reducing the exerted force from the sonographer. Similarly, [50] utilized an admittance controller to scale the force exerted by the user on the robot based on the environmental forces. The stability and adaptability of admittance-controlled robots facing different environmental forces were investigated in [16].

In the context of exoskeleton robots, [33] incorporated admittance control to generate a reference trajectory based on the measured force. To ensure stability in admittance-controlled robots, [13] analyzed and addressed unstable behaviors through an adaptive online method, tuning the admittance control gains. They stabilized the robot by monitoring high-frequency oscillations in the force signals. A similar approach was adopted in [31] for stabilizing admittance control during interactions with humans.

The combination of neural networks and admittance control for robot trajectory tracking was explored in [67], guaranteeing trajectory tracking using a neural network while employing admittance control to regulate torques and follow the desired trajectory. For a comprehensive overview of admittance control applications in robotics, [29] offers an insightful review.

2.3 Safe Motion Planning for Lower-limb Exoskeleton

The literature extensively investigates uncertainty analysis of Deep Neural Network (DNN) predictions for various applications, including medical ones [42]. Abdar *et al.* provide a comprehensive review of uncertainty quantification techniques in deep learning, while Ng *et al.* discuss the challenges of uncertainty estimation in medical applications [2], [44], [45]. Three main categories of uncertainty analysis in DNN predictions have emerged. The first involves learning model uncertainty alongside predictions, providing both a

prediction label and its corresponding uncertainty [6]. The second category considers the uncertainty introduced during DNN development, often implemented with dropout layers. Gal and Izmailov *et al.* propose a method for uncertainty analysis by modelling dropout layers using intrinsic dropout features [18], [19], [25]. Wen *et al.* introduce a layer called Flipout, inspired by dropout, for decorrelating gradients during training and estimating uncertainty [65]. Liu *et al.* demonstrate increased uncertainty awareness by incorporating weight normalization and a Gaussian Process in the output layer [36].

Additionally, out-of-distribution (OOD) analysis serves as a safety analysis method and can be considered an uncertainty analysis technique. Liu *et al.* use the distance between test samples and training data for OOD detection and uncertainty estimation in DNNs [30], [36]. Several other state-of-the-art OOD detection techniques are widely used, including the simple baseline method, ODIN, Mahalanobis, Outlier Exposure, and Likelihood-Ratio [23], [24], [32], [34], [58]. These methods, however, are not fast enough for real-time applications, such as within a robot's control loop. Therefore, this paper revisits these algorithms to make them real-time for integration into the robot control loop.

The proposed uncertainty analysis algorithm is evaluated in the context of a lower-limb exoskeleton. Central Pattern Generators (CPGs) are used for motion planning, offering time-continuous rhythmic motions similar to natural bipedal locomotion [59]. CPG has been investigated for exoskeleton trajectory planning in previous works [21], [39], [56], [60], [70]. DNNs have been employed in exoskeleton control for torque estimation and trajectory shaping [39], [59]. However, the reliability and safety of DNN predictions in unforeseen scenarios are crucial considerations, which the proposed method addresses by analyzing the trajectory-shaping algorithm's reliance on DNN predictions, ensuring exoskeleton safety during walking [5].

Chapter 3

Motion Planning for Ultrasound Breast Scanning[1]

3.1 Introduction

Ultrasound (US) is a widely used medical imaging modality known for its safety and cost-effectiveness compared to other imaging methods like MRI, CT, and X-ray, despite having a low signal-to-noise ratio. The quality of US images depends on various factors, including the intrinsic properties of the US machine, the orientation of the US probe during scanning, and the contact force with the tissue. While the US machine's intrinsic properties cannot be altered, a robotic system holding the US probe can address other factors to improve image quality.

Robot-assisted US scanning has gained significant attention, as it allows for the generation of high-quality images with automated control. Robotic US assistants can function in different modes: semi-autonomous, where they assist the sonographer through haptic feedback or partial probe control, and fully autonomous, where the robot controls all aspects of probe positioning and orientation during scanning based on acquired image quality, force data, or a predefined trajectory. The proposed method falls under the fully autonomous category, aiming for repeatable and reliable US scanning. In this chapter, we

[1]A version of this chapter has been presented as Akbari, M., Carriere, J., Sloboda, R., Meyer, T., Usmani, N., Husain, S. and Tavakoli, M., 2021, September. Robot-assisted Breast Ultrasound Scanning Using Geometrical Analysis of the Seroma and Image Segmentation. In 2021 IEEE/RSJ International Conference on Intelligent Robots and Systems (IROS) (pp. 3784-3791). IEEE.

present a fully-autonomous US image scanning algorithm.

Breast cancer is a prevalent disease among women aged 30 to 39, and various treatment options are available, including mastectomy and lumpectomy. Lumpectomy, followed by external beam radiation therapy, is a popular choice due to cosmetic reasons. After lumpectomy, a fluid-filled pocket called a seroma forms in the area where the tumor was removed. An alternative to external beam radiation therapy is permanent seed breast brachytherapy, which can be done in one or two sessions. However, precise needle insertion around the seroma is challenging, requiring accurate segmentation of the seroma during radiation therapy. To address this, our chapter proposes a method to control the probe during scanning to ensure the seroma remains in the field of view of the US images.

The proposed visual servoing algorithm controls five Degrees of Freedom (DoFs) of the probe during breast scanning. The algorithm has two phases, namely pre-scan and post-scan. During the pre-scan phase, we manually segment the seroma within the breast US images by moving the probe on the breast's surface to extract geometrical features. In the post-scan phase, which can be performed repeatedly, we calculate the desired probe position and orientation based on acquired US images to control the force and steer the probe for optimal seroma visualization. Our research aims to use an autonomous system for repeatable US post-scans, allowing for further required steps like 3D breast reconstruction. The setup is shown in Figure 4.1.

The outline of this chapter is as follows. We develop our proposed US scanning trajectory planning algorithm in Section 3.2 that uses pre-scan images for defining 5-DoF trajectory. We will propose our US visual servoing algorithm in post-scan in Section 3.3, which discusses the specific image features used to control both the position and orientation by updating the trajectory calculated in Section 3.2 of the probe during scanning. The experimental setup and results are presented in Section 3.4. Concluding remarks and discussions will be provided in Section 3.5.

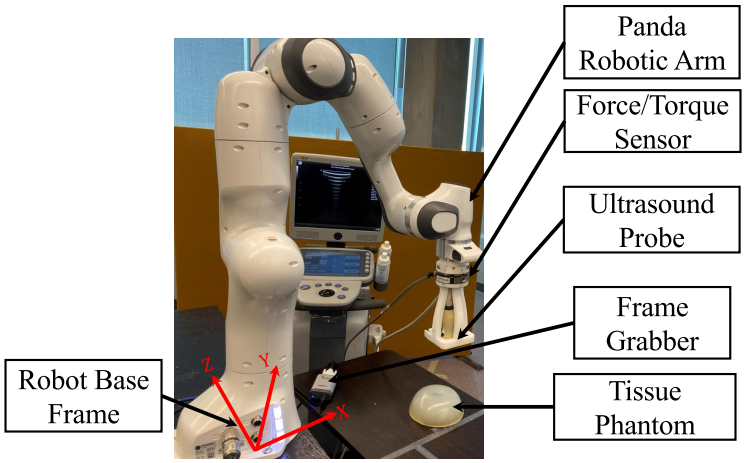

Figure 3.1: Robotic US scanning assistant including Panda robot arm, US probe, tissue phantom, frame grabber

3.2 Ultrasound Scanning Trajectory Planning

As previously mentioned, many factors need to be considered during US image acquisition to maintain the quality of the US image. Our proposed method consists of two phases, pre-scan to extract the initial trajectory and post-scan to refine the initial trajectory. The proposed system will extract necessary information from the breast and seroma during the pre-scan, including the location of the seroma inside the tissue. Our US image visual servoing algorithm will then control the US probe's orientation and position during the post-scan phase, utilizing the localized seroma from the pre-scan. The post-scan phase trajectory will be initially designed from this pre-scan information and real-time image processing and visual servoing will be used to refine the orientation and position of the probe throughout the post-scan.

3.2.1 Pre-scan Phase

In the pre-scan phase, the probe will be moved on the surface of the breast with an initial position and orientation trajectory either manually, by the sonographer, or through some naive autonomous US scan. The US image acquired at each point, and the position and orientation of the probe as determined from the robot encoders at each point will be saved for further processing. Within each of the pre-scan US images, the contour of the seroma (region of inter-

est) will be manually segmented. The manually segmented regions within the US images will be used to estimate the location and the shape of the seroma to design the post-scan trajectory. The seroma inside the breast will be approximated as an ellipsoid with frame $\{E\}$ that is defined along the principal axes of the ellipsoid. The dimensions of the ellipsoid are calculated using the manually segmented areas in the US pre-scan image set and principal component analysis. Before US scanning, calibration is done to determine the scale between pixel distances in the US images and real-word distances (in meters).

We will define various coordinate frames shown in Figure 3.2. These frames are defined to track the movement of the probe during post-scan and relate this movement to each other for estimating the location and shape of the seroma for post-scan. We are going to find the ellipsoid frame $\{E\}$ in space from the pre-scan images centered at the center of the ellipsoid approximated from these images and aligned with principal axes of the ellipsoid. We define intersecting frame $\{C\}$ to calculate the desired value of out-of-plane rotation in this frame that would simplify the calculation. We also introduce US image frame as $\{U\}$ for each pixels value in the image and US probe frame (desired frame) $\{D\}$ to relate the movement of the US probe with respect to other frames attached to the system and acquired features from US image in our proposed control scheme. We can then estimate the dimension of the seroma by a transformation of each point belonging to the segmented region in a pre-scan image to the base frame, i.e, transforming from $\{U\}$ to the $\{B\}$. The mathematical details in calculating frame transformation from $\{E\}$ and $\{U\}$ to $\{B\}$ are ${}^{B}P = {}^{B}_{U}T\,{}^{U}P$, ${}^{B}P = {}^{B}_{E}T\,{}^{E}P$. Transformation matrix from $\{B\}$ to $\{D\}$, which is important for our control system is shown as

$$ {}^{D}_{B}T = \left(\begin{array}{ccc|c} & R(\alpha,\beta,\gamma) & & \begin{array}{c} {}^{D}P_{x_0} \\ {}^{D}P_{y_0} \\ {}^{D}P_{z_0} \end{array} \\ \hline 0 & 0 & 0 & 1 \end{array}\right), \tag{3.1} $$

where $[{}^{D}P_{x_o}, {}^{D}P_{y_o}, {}^{D}P_{z_o}]$ is the position of the origin of $\{B\}$ in $\{D\}$.

In Figure 3.2, we have shown the position and orientation of the probe during the pre-scan phase.

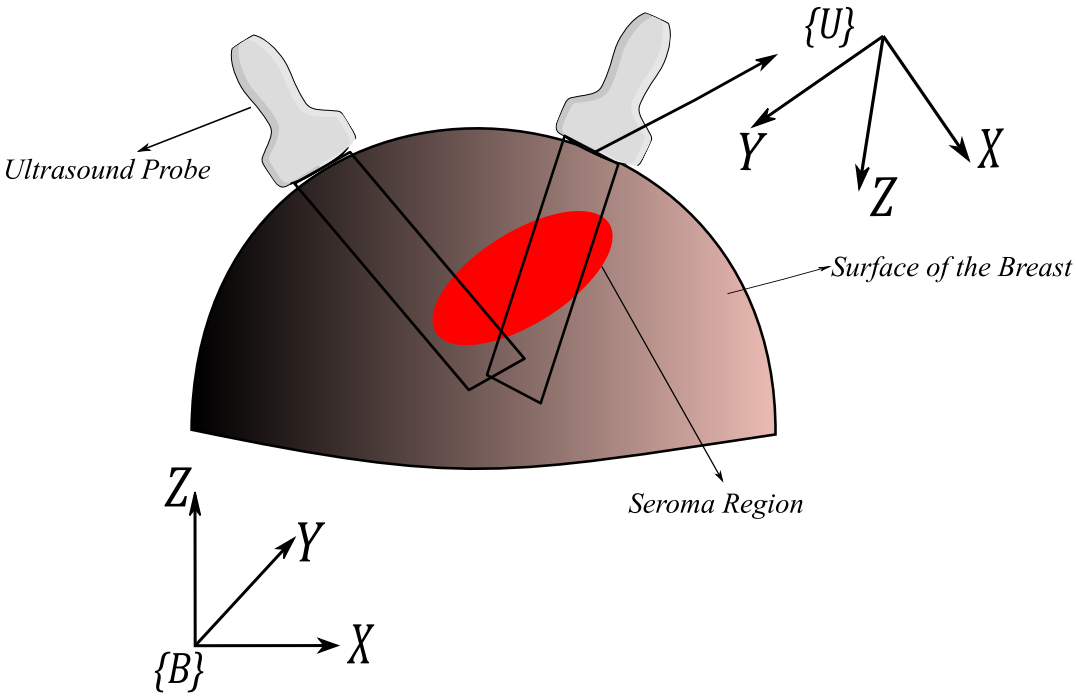

Figure 3.2: Visualization of frames attached to the system in pre-scan phase

3.2.2 Post-scan Phase

The geometrical information of the ellipsoid calculated in the pre-scan phase is being used for calculating the desired values of in-plane, out-of-plane, and $x-y-z$ position of the probe. We are using an axial plane for taking images, which is perpendicular to the trajectory. Hence, we define the orientation of the probe in this plane as in-plane rotation and the orientation of the probe out of this plane as out-of-plane rotation. We update the in-plane rotation and the movement of the probe in the z direction of the $\{B\}$, as shown in Figures 3.2 and 3.3, by segmenting the seroma and using an image confidence map.

Designing Trajectory for Post-scan

We calculate the desired $x-y-z$ trajectory of the probe on the surface of the breast based on the intersection of a plane containing the principal axis of the ellipsoid (i.e. aligned with the principal axis ${}^{E}x$ of the seroma) and oriented with the orientation of the this principal axis to have maximum alignment with surface normal of the breast surface. The post-scan trajectory will then

be a curve on the surface of the breast resulting from this intersection. We can define our trajectory points as ${}^{B}P_j = [{}^{B}x_j, {}^{B}y_j, {}^{B}z_j, \alpha_j, \beta_j, \gamma_j]$, which creates a set of point $\Pi = \{{}^{B}P_j | j = 1, \ldots, n\}$. γ or the roll angle of the probe is the part of the trajectory that does not affect our scanning method, hence we are not considering it in our control scheme. The beginning and endpoint of the trajectory are defined as ${}^{B}P_0$ and ${}^{B}P_n$, respectively, and are chosen manually on the intersecting curve. The visualization of the frame attached to the system and acquired trajectory is shown in Figure 3.3.

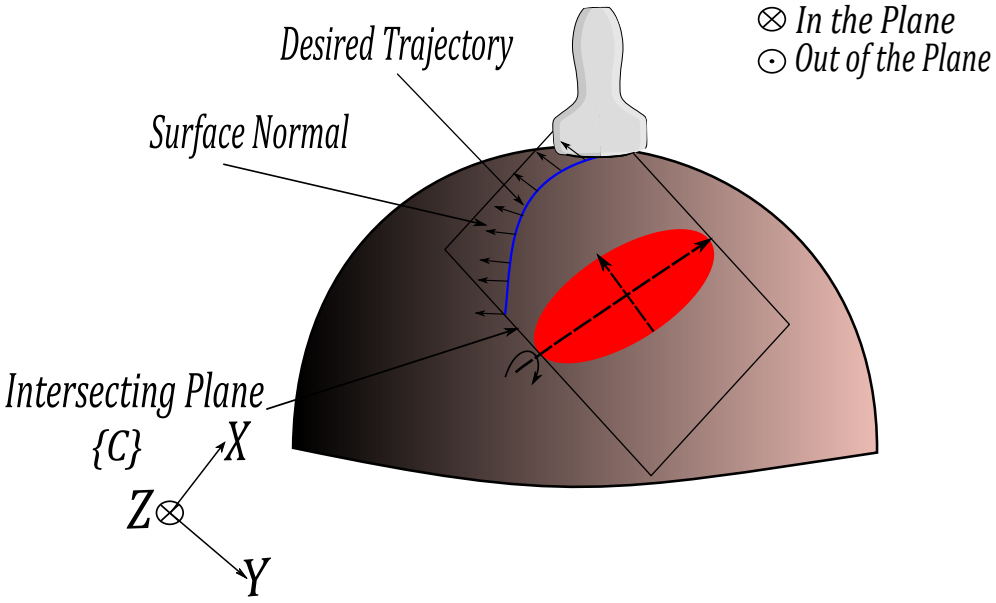

Figure 3.3: Designing Trajectory for post-scan phase

The geometrical dimensions of the ellipsoid, containing the seroma, inside the breast are shown in an axial view in Figure 3.4a and a sagittal view in Figure 3.4b. Here, the view is defined as a projection of the in two planes from the user view. The desired out-of-plane α_j and in-plane β_j rotations for points j on the trajectory will be found using geometrical analysis based on the ellipsoid and the surface of the breast.

Finding Desired Out-of-plane Orientation

The intersecting plane frame $\{C\}$, containing the principal axis of the ellipsoid, allows for finding α_j. The desired out-of-plane rotations are designed to sweep the US probe smoothly as it is translated along the trajectory so that the US

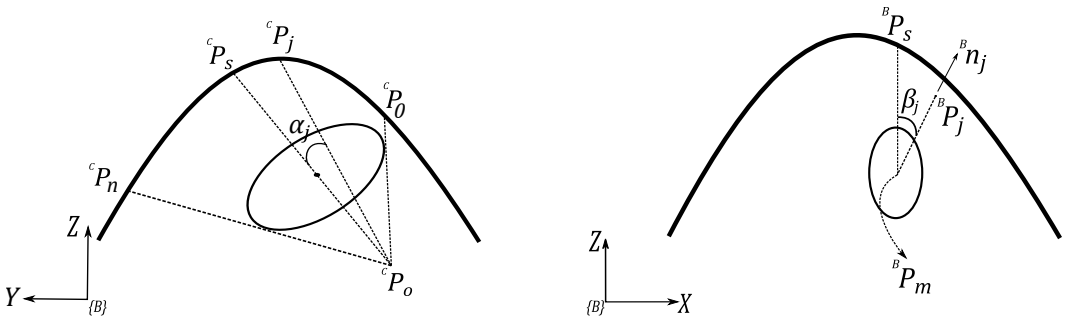

(a) Finding α_j using axial view (b) Finding β_j using sagittal view

Figure 3.4: Finding α_j and β_j using axial and sagittal view

probe is always pointed towards a target point ${}^{C}P_O$. The point ${}^{C}P_o$ is the point that the line passing through the center of ellipsoid from the surface of the breast intersect with two separate tangents originated from beginning and end point of the trajectory. The visualization of the points coordinates that need to be defined for calculating α_j are shown in Figure 3.4a. We define the coordinates of the following points in $\{C\}$ using ${}^{C}_{B}T = {}^{B}_{C}T^{-1}$ as ${}^{C}P_o = {}^{C}_{B}T\,{}^{B}P_o$, ${}^{C}P_n = {}^{C}_{B}T\,{}^{B}P_n$, ${}^{C}P_s = {}^{C}_{B}T\,{}^{B}P_s$ and ${}^{C}P_j = {}^{C}_{B}T\,{}^{B}P_j$.

The desired value of out-of-plane rotation α_j can be found in

$$\begin{aligned}\alpha_j = \text{atan2}({}^{C}z_s - {}^{C}z_o, {}^{C}y_s - {}^{C}y_o) \\ - \text{atan2}({}^{C}z_j - {}^{C}z_o, {}^{C}y_j - {}^{C}y_o)\end{aligned} \tag{3.2}$$

between ${}^{C}P_j$, ${}^{C}P_s$ and ${}^{C}P_o$.

Finding Desired In-plane Orientation

With the out-of-plane orientation α_j of the US probe trajectory defined, we can find the desired value for the in-plane orientation β_j. This process is shown in a sagittal view of the breast in Figure 3.4b. Here, we are using the center of ellipsoid ${}^{B}P_m$ which was also found from the pre-scan images.

We define ${}^{B}P_s$, ${}^{B}P_j$, and ${}^{B}P_m$ in the robot base frame $\{B\}$ to calculate desired in-plane orientation. We need to consider surface normal vectors of the breast when finding the desired value of β_j so that the probe is kept in a natural orientation, with respect to the surface of the breast, during scanning.

This is shown in

$$\begin{aligned} \beta_j = & \max_i \quad \vec{\beta_i} \cdot {}^B\vec{n}_i \\ & \text{subject to} \quad i = 1, \ldots, \theta. \end{aligned} \tag{3.3}$$

that finds the angle which maximizes the dot product between the normal vector and the candidate vectors ($\vec{\beta}$) in a feasible range $(1, \ldots, \theta)$. The feasible range can be found by considering the dimension of the probe and the region of interest in each point of the trajectory found in 3.2.2. The surface normal vector ${}^B\vec{n}_j$ of the breast in position ${}^BP_j$ within the scanning trajectory is

$${}^B\vec{n}_j = \begin{bmatrix} \frac{\partial f({}^Bx_j, {}^By_j)}{\partial x} \\ \frac{\partial f({}^Bx_j, {}^By_j)}{\partial y} \\ -1 \end{bmatrix}, \tag{3.4}$$

Which considers the points on the surface of the breast follows the 3D equation as

$${}^Bz_j = f({}^Bx_j, {}^By_j). \tag{3.5}$$

3.3 Ultrasound Visual Servoing

From Section 3.2, we have developed a 5-DoF trajectory on the surface of the breast for the robot US scanning assistant to follow. The five DoFs are the $x - y - z$ position of the probe, and the in-plane and out-of-plane rotation of the probe on the surface of the breast. Using visual servoing techniques, we now refine the in-plane angle β_j of the probe and the downward pressure applied to tissue (by modulating ${}^Dz_j$) according to information from the US image confidence map and the segmentation of seroma in the US frame.

US images have a low signal-to-noise ratio and need preprocessing to enhance their quality to be used for control purposes. The US confidence map is a commonly used preprocessing method. The US confidence map is a per-pixel measure calculating the probability of a random walk [20] starting from each pixel to reach a number of virtual transducer elements, under specific US constraints [28]. This method considers an US image as a graph where nodes represent the pixels with edges interconnecting the nodes. For our implementation of the confidence map, we will consider a 4-connected neighborhood for each pixel node.

The mean value of the confidence map C_{mean_j} can be considered as an image-based measure of the contact between the breast tissue and the US probe. The desired value of the mean of the confidence map is defined as C_{set}. The C_{set} value can be defined experimentally during the pre-scan phase ensuring the contact between the probe and the breast is sufficient. The ${}^{D}z_j$ position from the previously found trajectory is updated, in real-time, to increase C_{mean_j} to C_{set} to ensure sufficient probe/tissue contact. The mathematical equation for calculating C_{mean_j} is

$$C_{mean_j} = \frac{1}{M \times N} \sum_{(p_x,p_y)\in S} C(p_x, p_y) \tag{3.6}$$

where S is the area of the US confidence map, M and N are the height and width of S, and $C(p_x, p_y)$ is the confidence value of pixel located in (p_x, p_y). The error between current and desired value ($e_{c_j} = C_{mean_j} - C_{set}$) is used as an input to the controller for controlling the ${}^{D}z_j$ about the original ${}^{D}z_j$ position calculated in Section 3.2.

The center of the mass of the segmented object is a measure that indicates whether the image intensities are well divided over the segmented region or not. We use this feature to refine our predefined in-plane rotation in the scanning. Here, a US image I_j will be segmented for extracting the seroma. The output is a binary image, in which the background intensities have 0 values and foreground intensities are 1. The center of mass of the segmented image is a measure for rotating the probe toward the seroma during scanning. We calculate the location of the center of mass in the segmented image as

$$\begin{aligned} {}^{U}\mu_i &= \frac{1}{I_{tb}} \sum_{(i,j)\in I_b} i \times I_b(i,j) \\ {}^{U}\mu_j &= \frac{1}{I_{tb}} \sum_{(i,j)\in I_b} j \times I_b(i,j). \end{aligned} \tag{3.7}$$

Here, ${}^{U}\mu_i$ and ${}^{U}\mu_j$ are the coordinate of the center of mass in $\{U\}$, I_b is the binary segmented image, and $I_{tb} = \sum_{(i,j)\in S} I_b(i,j)$. Our segmentation algorithm uses Otsu's threshold method to create a binary image and selects the largest connected component as the seroma inside the breast. The values

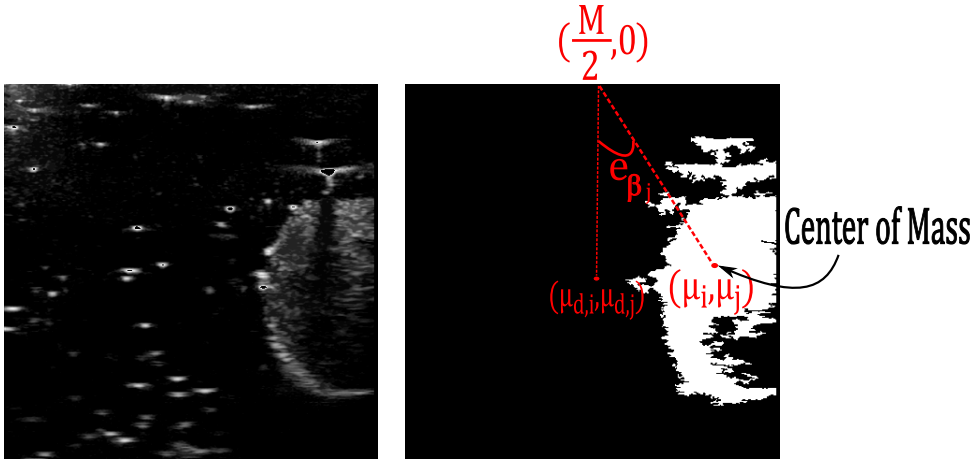

Figure 3.5: Center of the mass and calculation of e_{β_j} using segmented US frame

of ${}^{U}\mu_i$ and ${}^{U}\mu_j$ can be transferred to $\{D\}$, resulting in ${}^{D}\mu_x$ and ${}^{D}\mu_y$ (${}^{D}\mu_x = {}^{D}_{U}T\,{}^{U}\mu_i$ and ${}^{D}\mu_y = {}^{D}_{U}T\,{}^{U}\mu_j$). The angle between the central image scan line and the line passing through the center of the mass as determined from the center of the scan line defines an error that can be used to control the in-plane rotation of the probe during scanning. The mathematical expression for finding the in-plane rotation error e_{β_j} is

$$\begin{aligned} e_{\beta_j} = \text{atan2}({}^{U}\mu_j - \frac{M}{2}, {}^{U}\mu_i) - \\ \text{atan2}({}^{U}\mu_{d,j} - \frac{M}{2}, {}^{U}\mu_{d,i}) \end{aligned} \tag{3.8}$$

where ${}^{U}\mu_{d,i}$ and ${}^{U}\mu_{d,j}$ are the coordinate of desired value. A visual illustration of how the value e_{β_j} is calculated is shown in Figure 3.5.

3.3.1 Ultrasound Scanning Robot Controller

From the trajectory found in Section 3.2 and the visual serving information demonstrated in Section 3.3, we can now describe our control law for the position and orientation of the US probe during the post-scan. This controller considers the position and orientation of the probe in $\{D\}$ as ${}^{D}P = [{}^{D}x_p, {}^{D}y_p, {}^{D}z_p, {}^{D}\alpha_p, {}^{D}\beta_p, {}^{D}\gamma_p]^t$. The desired value of the robot's position and orientation in $\{D\}$ is denoted as ${}^{D}P_d = [{}^{D}x_d, {}^{D}y_d, {}^{D}z_d, {}^{D}\alpha_d, {}^{D}\beta_d, {}^{D}\gamma_d]^t$. Here, the initial $x - y - z$ position of a trajectory calculated from Section 3.2.2.

The initial and desired value of in-plane rotation and out-of-plane rotation for any points of the trajectory are β_j and α_j respectively, which were calculated in Section 3.2.2 and 3.2.2. The desired value of the probe position in the z direction ${}^{D}z_j$ and in-plane rotation will also be updated using e_{c_j} and e_{β_j} as ${}^{D}z_d = {}^{D}z_d + k_1 e_{c_j}$, ${}^{D}\alpha_d = {}^{D}\alpha_d + k_2 e_{\beta_j}$. The error between the current point and the desired one is being used for controlling the robot during scanning calculated by

$$ {}^{D}P_d = \begin{bmatrix} {}^{D}x_d \\ {}^{D}y_d \\ {}^{D}z_d + k_1 e_{c_j} \\ \alpha_j \\ \beta_j + k_2 e_{\beta_j} \\ {}^{D}\gamma_d \end{bmatrix}, {}^{D}E_j = \begin{bmatrix} {}^{D}x_d - {}^{D}x_p \\ {}^{D}y_d - {}^{D}y_p \\ {}^{D}z_d + k_1 e_{c_j} - {}^{D}z_p \\ \alpha_j - {}^{D}\alpha_p \\ \beta_j + k_2 e_{\beta_j} - {}^{D}\beta_p \\ {}^{D}\gamma_d - {}^{D}\gamma_p \end{bmatrix} \tag{3.9} $$

Here, k_1 and k_2 are gains assigned to the corresponding features to relate them to the velocity of the robot.

The error ${}^{D}E_j$ is an input to a PID controller to control both the position and orientation of the probe during scanning. The image acquisition block, which is a US machine, sends an image to the receiver for calculating C_{mean_j} and e_{β_j} by using confidence map mean from (3.6) and the segmented center of mass from (3.7). The control loop is shown in Figure 4.9 and the algorithm is demonstrated in Algorithm 2, where ϵ, δ_1, and δ_2 are the tolerance of the position and orientation error in the proposed system.

3.4 Experiment and Results

In this study, an Axia80-M20 force-torque sensor (ATI Industrial Automation, Apex, NC, USA) is mounted on a Panda robotic arm (Franka Emika GmbH, Munich, Germany) and an adapter was built to hold an US probe (see Figure 4.1). The US machine used for the experiment was an Ultrasonix Touch with a 4DL14-5/38 Linear 4D transducer (Ultrasonix Corp, Richmond, BC, Canada). For this experiment, we only used the 2D functionality of the US probe. Images from the US machine were captured in real-time with an Epiphan DVI2USB3.0 (Epiphan Systems Inc, California, USA) for processing. For our experiment, we used a tissue phantom made of plastisol.

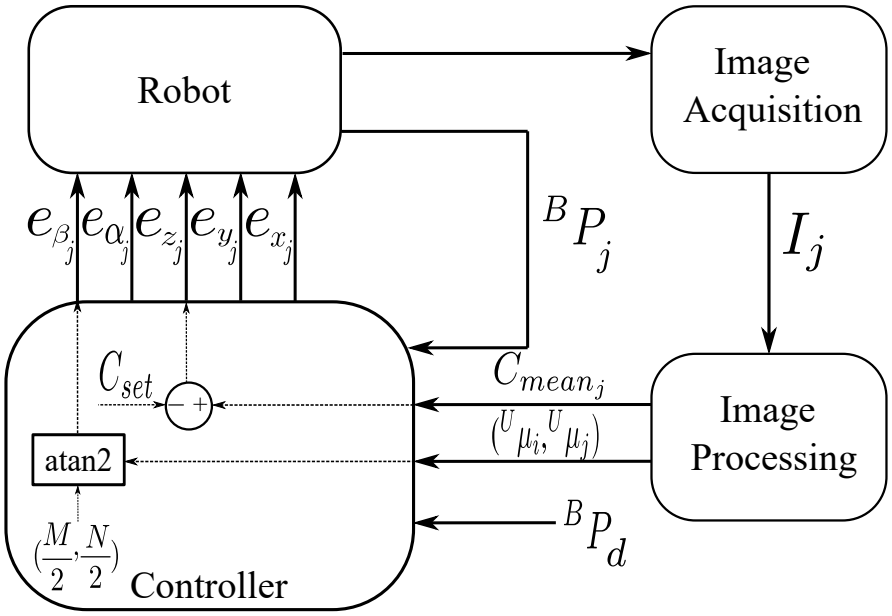

Figure 3.6: Control loop of post-scan phase

The controller was programmed and implemented in MATLAB 2019a (The Mathworks Inc, Natwick, MA, USA) and ran using Simulink on a PC running Ubuntu 16.04 LTS. The PC has an Intel Core i5-8400 running at 4.00 GHz. The communication between robot and computer was done over UDP.

The pre-scan phase consisted of moving the US probe on the surface of the phantom tissue and recording the applied forces and US probe positions. The duration of the pre-scan phase depends on the size of the breast and whether the location of the seroma has been extracted or not. The seroma within this initial image set was manually segmented and the parameters, including the principal axis and center, of the approximated seroma ellipsoid, was found. We designed our post-scan trajectory based on the output of the pre-scan phase. During the post-scan phase, the robot moved the probe along the surface of the phantom and the algorithm changed the values of $x - y$ position, α_j, β_j and force applied to the surface of the phantom. The evaluation is based on three main criteria, which are reported in Figure 3.7 for five randomly selected points on the trajectory, with five different desired out-of-plane and in-plane rotations, on the surface of the phantom calculated using(3.2) and (3.3). The evaluation metrics are the norm of the error in the probe's orientation with

Algorithm 1 Proposed US Scanning Controller

Require: Desired position and orientation of the probe of the probe $({}^{D}x_d, {}^{D}y_d, {}^{D}z_d, {}^{D}\alpha_d, {}^{D}\beta_d, {}^{D}\gamma_d)$, ϵ, δ_1, δ_2

while $e_{c_j} \geqslant \epsilon$ and $e_\alpha \geqslant \delta$ and $e_\beta \geqslant \delta_2$ **do**
  if $e_{c_j} \leqslant \epsilon$ **then**
    Update the ${}^{D}z_d$
    $e_{c_j} = C_{mean_j} - C_{set}$
  end if
  if $e_\alpha \geqslant \delta_1$ and $e_\beta \geqslant \delta_2$ **then**
    Update ${}^{D}\alpha_d$ using (3.2)
    $e_\alpha = {}^{D}\alpha_d - \alpha_j$
    Update the ${}^{D}\beta_j$ using (3.3) and (3.8)
    $e_\beta = {}^{D}\beta_j - \beta_j$
  end if
end while

respect to the desired in-plane and out-of-plane rotation as

$$\|e_{\alpha,\beta}\|^2 = \|({}^{D}\alpha_p - {}^{D}\alpha_d, {}^{D}\beta_p - {}^{D}\beta_d)\|^2, \tag{3.10}$$

the variation of β_j which results in movement of the center of mass, and the force applied to the phantom during the experiment.

The variation of error norm $\|e_{\alpha,\beta}\|^2$ reported in Figure 3.7 shows our proposed method is able to decrease the norm of the error in each point of the trajectory. It also indicates that our method works even when there is a change in the in-plane rotation caused by the movement of the center of mass. Figure 3.7 shows our proposed controller compensates for deviation of the probe orientation caused by the movement of the center of mass, with the probe being reoriented successfully to keep the center of mass on the center of an image frame. This guarantees that our proposed method keeps the seroma in the center of the acquired US image as the variation converges to 0 for each point. The force values reported in the last figure of Figure 3.7 show that our proposed method applies a reasonable amount of force during scanning (The values are different for different points as they correspond to different parts of the tissue phantom with different characteristics). This level of force does not cause deformation of the tissue during scanning. We have also calculated the average of these criteria for the five points within Table 4.1.

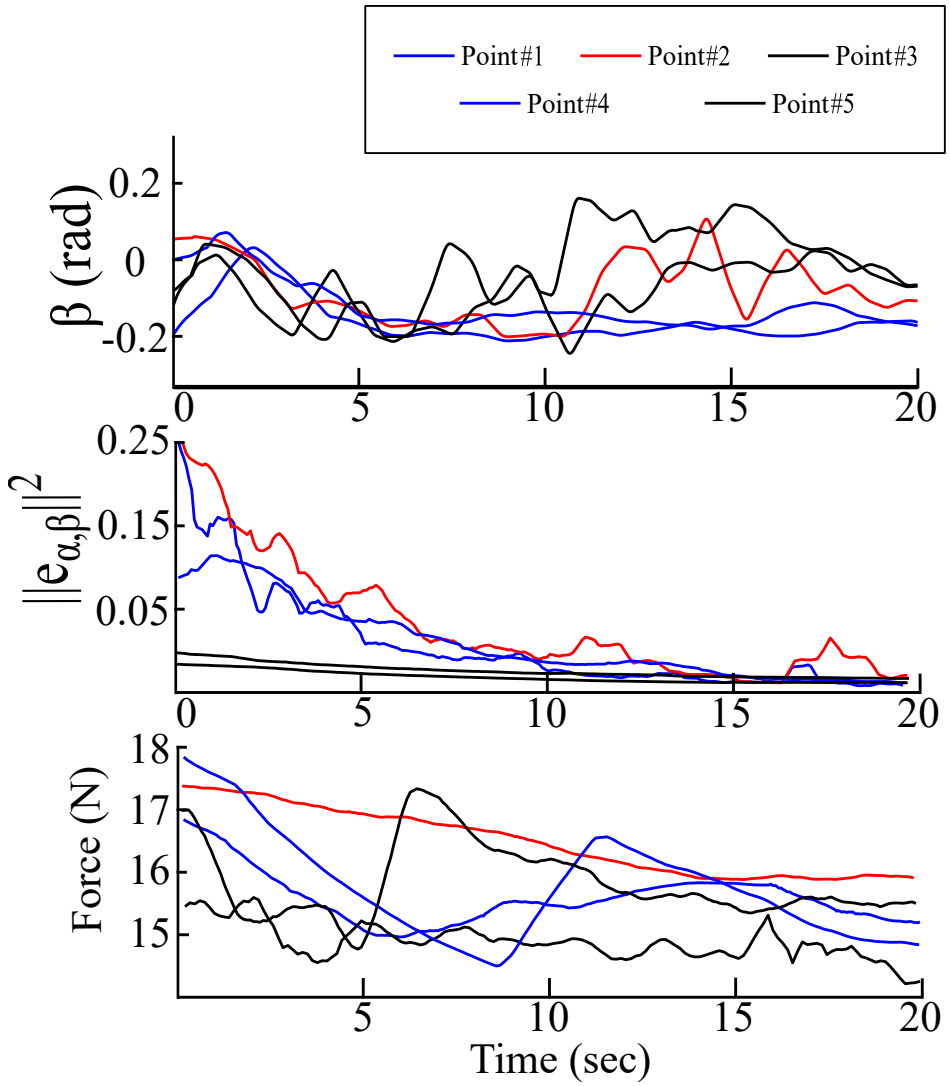

Figure 3.7: Experimental results for variation of β, $\|e_{\alpha,\beta}\|^2$ and force

3.5 Conclusion

In this chapter, we proposed a method to define a 5-DoF US scanning trajectory based on the geometrical features of a target seroma within the breast. A visual servoing algorithm method was used to update two of the controlled DoFs in real-time during scanning to ensure sufficient probe contact and to better visualize the seroma within the US images. Our proposed trajectory generation and visual servoing method, referred to as the post-scan, was based on information captured during a manual pre-scan set of images. The pre-scan images can be captured at arbitrary orientations and positions, with the pose

Table 3.1: Average of $\|e_{\alpha,\beta}\|^2$, deviation of β_j and force values in five separate points on the trajectory

Point	$\|e_{\alpha,\beta}\|^2$	Deviation of β_j	Force
Point #1	0.04± 0.048	-0.19± 0.015 (rad)	16.01± 0.314 (N)
Point #2	0.07± 0.057	-0.06± 0.021 (rad)	16.84± 0.397 (N)
Point #3	0.01± 0.007	0.01± 0.021 (rad)	15.31± 0.217 (N)
Point #4	0.06± 0.022	-0.06± 0.016 (rad)	16.14± 0.645 (N)
Point #5	0.01± 0.006	-0.02± 0.019 (rad)	16.20± 0.455 (N)

of the US probe was recorded as the pre-scan images are capture. The pre-scan images were processed to extract geometrical information of the seroma inside the breast. The seroma was approximated by an ellipsoid, with the center of the ellipsoid and principal axis being used as part of the geometrical analysis to define the post-scan trajectory. For the post-scan, we calculated the desired US probe trajectory through the intersection of a plane (containing the ellipsoid principal axis) with the surface of the breast. The intersection points on the surface of the breast then form the desired $x - y - z$ trajectory of the US probe. The in-plane and out-of-plane rotation of the probe is calculated at each point of the trajectory via geometrical analysis of the seroma inside of the breast. The in-plane orientation of the probe is updated using an online segmentation algorithm that locates the center of the seroma and orients the probe to point towards it. The desired value of the z position of the probe was also updated, using the average confidence map calculated from the US image during scanning, to ensure sufficient contact between the breast and the probe. The proposed method was evaluated experimentally using plastisol phantoms. The experimental results show that our proposed method orients the probe to keep the seroma in the center of acquired image and keeps the probe in contact with the phantom with minimum deformation.

In the future, we will work on a 3D reconstruction algorithm that is able to generate a 3D volume of the breast using pre-scan images automatically to be able to control the remaining DoF of the robot during visual servoing. This additional information will help the proposed method locate the seroma more

precisely for the post-scan phase. The other feature that can be added to the system is to propose a new set of features that is able to control the probe when a needle is inserted inside the breast to have a good visualization of the seroma and needle together during scanning.

Chapter 4

Motion Planning based on Ultrasound Image Quality Assessment[1]

4.1 Introduction

As mentioned in Section 3.1, ultrasound (US) imaging is a widely used and safe medical modality, known for its radiation-free nature, cost-effectiveness, and wide availability. Amid the COVID-19 pandemic, US scanning has become a vital tool for COVID-19 diagnosis, especially in resource-limited areas where access to lab kits is limited [7], [38]. However, certain factors related to US scanning during the pandemic need to be addressed. Firstly, the close contact between sonographers and patients poses a significant risk of virus transmission [26], [27], [40], [73]. Secondly, COVID-19 patients with underlying conditions, such as heart conditions, require careful US imaging, like echocardiography. Lastly, US imaging can be time-consuming, with most scans lasting between 15 to 45 minutes [46]. To mitigate these challenges, this chapter proposes a quick, low-cost, and deployable solution using robots to assist in US scanning. Robots can handle tasks that put the sonographer at higher risk, while experienced sonographers manage critical aspects of the scanning process. This approach significantly reduces the risk of virus transmission, as the robotic system can

[1]A version of this chapter has been published as Akbari, M., Carriere, J., Meyer, T., Sloboda, R., Husain, S., Usmani, N. and Tavakoli, M., 2021. Robotic ultrasound scanning with real-time image-based force adjustment: quick response for enabling physical distancing during the COVID-19 pandemic. Frontiers in Robotics and AI, 8, p.645424.

be easily sanitized between procedures [62].

In developing robotic US scanning, image quality assessment plays a crucial role. Medical image quality assessment has been a challenging topic, and various methods have been proposed in the literature. There are three categories of image quality assessment algorithms based on the availability of reference images or supplementary information. The first category is full-reference image quality assessment, where a reference image is available, and the quality metric compares a given image to the reference image. The second category is semi-reference image quality assessment, which utilizes limited information about the reference image, such as critical features. For example, [11] uses visual features for sonar image quality assessment, even without a reference image. Semi-reference methods are more challenging and require careful handling of additional information. The final category is no-reference image quality assessment, where the algorithm lacks access to a reference image or any related information. This category is particularly challenging but crucial for medical image quality assessment [12]. Since quality reference images are typically unavailable, the key aspect of no-reference image quality assessment is developing appropriate quality metrics based on relevant features present in high-quality and low-quality images.

The inherent noise in US images complicates the image processing and makes US image quality assessment challenging. In this chapter, we propose a method to assess the US image quality while a robotic arm holds the US probe. The algorithm will be integrated into the robot control loop for automated tissue scanning. An admittance-based controller will be employed for the robot to automatically control the scanning force applied to the tissue by the US probe [17], [69]. The US scanning assistant setup is shown in Figure 4.1. The sonographer will use a handle to position the robot, utilizing the robot's built-in admittance control, while the robot will adjust the scanning force based on the quality analysis of the acquired image. This system reduces contact time and minimizes the risk of virus transmission between the sonographer and the patient, as the robot autonomously performs the scanning process based on image quality assessment feedback.

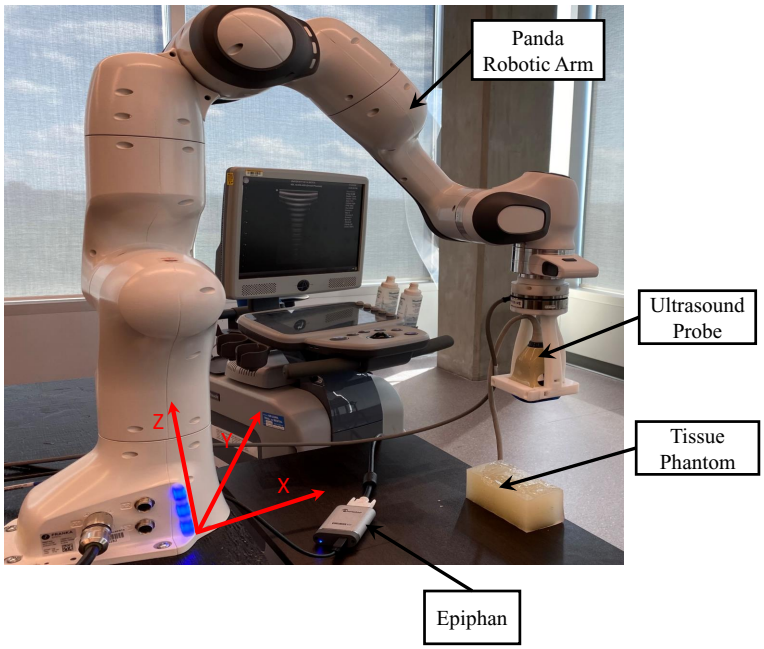

Figure 4.1: US scanning assistant including Panda robot arm, US probe, handle for sonographer, tissue phantom, frame grabber, and robot base frame

The outline of the chapter is as follows. We develop our proposed image quality assessment algorithm in Section 4.2 by giving details of the algorithm and discussing the specific image features it uses. In Section 4.3, we will give the details of the robotic admittance controller used in the system to adjust the US scanning force applied to the tissue. The experimental setup and the experimental results are presented in Section 4.4. We will conclude our method and its advantages in Section 4.5.

4.2 Image Quality Assessment Algorithm

As previously mentioned, US images are usually very noisy, and therefore, the tissue is not very clear in the images. This problem makes the automated assessment of US images complicated. A US image quality assessment algorithm should distinguish between different features in an image and decide on image quality based on the acquired features. For our proposed image quality

assessment method, we will use a Support Vector Machine (SVM) classifier, which is compatible with small training sets and has proven to have a good ability to solve complicated problems, especially in medical applications.

4.2.1 Image Quality Assessment Metrics

We propose three distinct features for estimating the quality of the image. The first feature is based on the contact between the probe and the tissue. The second feature computes the level of compression caused by the US scanning force applied to the tissue. The third feature is an estimation of the noise level in the image. The noise level is estimated based on the statistical features of the noise in the US image. We will discuss each of the features in-depth in the following sub-sections.

Correlation

We use image correlation for modelling the contact between the tissue and probe. When there is no contact (or proper contact) between the probe and tissue, the US image will only consist of patterns of arcs; see Figure 4.2a. When we have sufficient contact, however, actual tissue will be visible in the image. In Figure 4.2a, the image captured by the US machine was defined as no-contact image I_{nc} in the sense that probe is not contacting the tissue when the image is captured. We define the contact feature as the correlation of no-contact image I_{nc} with an image captured by the US machine I_k in every time step k of the experiment. The contact feature c_k gives us a good estimation of the sufficiency of contact and $c_k \in [0, 1]$. The mathematical details of how the correlation between the images is calculated and how contact between the probe and the tissue is defined are as follows:

$$\text{corr}(I_k, I_{nc}) = \frac{\sum_{p_x=1}^{M}\sum_{p_y=1}^{N}(I_k(p_x,p_y)-\overline{I_k})(I_{nc}(p_x,p_y)-\overline{I_{nc}})}{\sqrt{(\sum_{p_x=1}^{M}\sum_{p_y=1}^{N}(I_k(p_x,p_y)-\overline{I_k})^2)(\sum_{p_x=1}^{M}\sum_{p_y=1}^{N}(I_{nc}(p_x,p_y)-\overline{I_{nc}})^2)}} \tag{4.1}$$

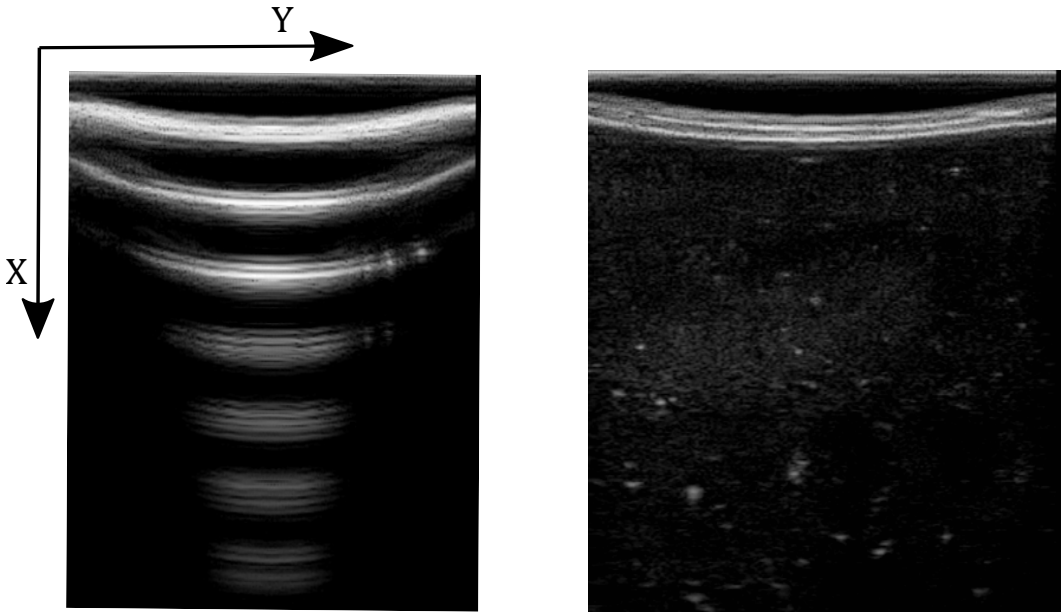

(a) Ultrasound image without sufficient contact

(b) Ultrasound image with sufficient contact

Figure 4.2: Ultrasound images with and without contact between tissue and probe

$$c_k = \begin{cases} 1, & \text{if } \text{corr}(I_k, I_{nc}) \geq t_{corr} \\ 0, & \text{if } \text{corr}(I_k, I_{nc}) < t_{corr} \end{cases} \tag{4.2}$$

Here, the contact feature c_k is the value of the correlation between the two images. (p_x, p_y) is the location of pixels in the image frame, and M and N are the height and width of input images, respectively. $\overline{I_k}$ and $\overline{I_{nc}}$ are the average of the pixels' intensities in the acquired image and the image with no contact with the tissue, respectively, and t_{corr} is the threshold for determining the contact level. Figure 4.2 shows two images, in which Figure 4.2a was captured when there is not enough contact between the tissue and the probe, and Figure 4.2b was conducted with sufficient contact. The x-y axis in the image frame is shown in Figure 4.2a and it is the same for all images in this chapter.

Compression

The level of compression is a very important feature in US image acquisition. When the robot applies force to the tissue, it causes deformation. More force causes greater distortion/deformation. This causes pain for the patient, and

may lead to wrong clinical diagnosis [15]. The proposed compression feature is the difference between the maximum and minimum index of the pixels brighter than the threshold t_{comp}, relative to the image's size in the vertical direction. The mathematical expression for calculating the image compression feature is as follows:

$$\begin{aligned} U &= \max(p_y), \text{ where } I_k(p_y, \forall p_x \in I_k) \geq t_{comp} \\ L &= \min(p_y), \text{ where } I_k(p_y, \forall p_x \in I_k) \geq t_{comp} \\ f_c &= \frac{U - L}{M} \end{aligned} \tag{4.3}$$

In (4.3), U and L are the maximum and minimum location of the pixels having intensity higher than t_{comp}. We define f_c as the compression feature in (4.3). M is the height of the image along the y direction. Figure 4.3 shows two images with different levels of compression. Figure 4.3a is the US image with a high level of compression, and Figure 4.3b is the US image with a low level of compression. We have also shown a variation of f_c with respect to measured force in the z direction of the force sensor frame $F_{Z|k}$ (this is aligned with the y direction in image frame) in Figure 4.4.

Noise

As we mentioned earlier, the US image is very noisy. The noise comes from the manner in which US captures an image. This noise feature is also very important for the quality assessment of US images. As a first step, we use a Wiener filter for removing speckle noise from the US image. The calculation of the Wiener filter is based on [35]. The US image's noise level can be estimated by the mean and standard deviation of the difference image between the original image I_k and the filtered image $I_{k,f}$. (4.4) to (4.8) show the mathematical explanation of using a Wiener filter to remove noise from the US image and calculate the noise feature.

$$\mu = \frac{\sum_{p_x \in \eta} \sum_{p_y \in \eta} I_k(p_x, p_y)}{P \times Q} \tag{4.4}$$

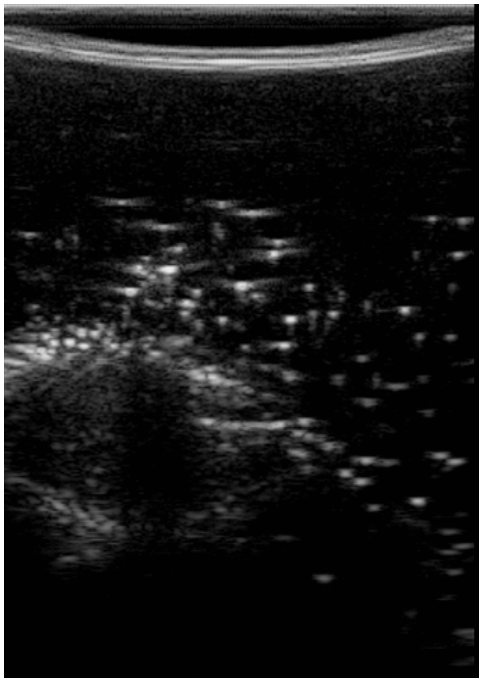

(a) Ultrasound image with high tissue compression

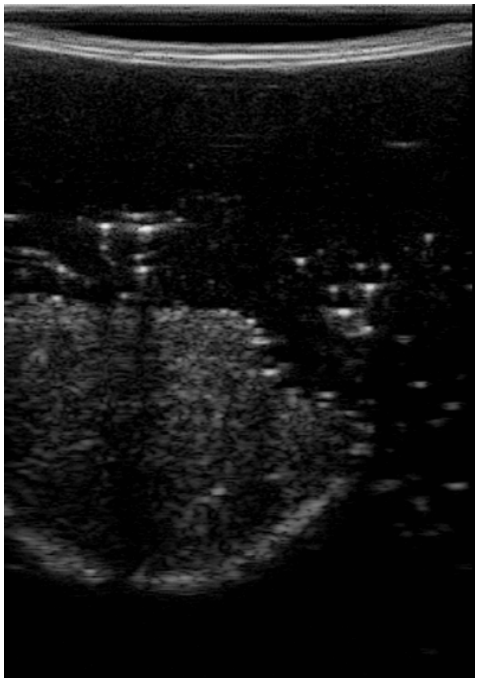

(b) Ultrasound images with low tissue compression

Figure 4.3: Ultrasound images with high and low level of compression

$$\sigma^2 = \frac{\sum_{p_x \in \eta} \sum_{p_y \in \eta} I_k(p_x, p_y)^2}{P \times Q} - \mu^2 \tag{4.5}$$

$$I_{k,f}(p_x, p_y) = \mu + \frac{\sigma^2 - \nu^2}{\sigma^2}(I_k(p_x, p_y) - \mu) \tag{4.6}$$

$$I_n = I_k - I_{k,f} \tag{4.7}$$

$$f_n = \overline{I_n} + \sigma_n \tag{4.8}$$

Here, η is the neighbourhood with the size of $P \times Q$ around each pixel of the noisy image and $I_k(p_x, p_y)$ is the intensity of each pixel in the noisy US image. μ is the average of pixel intensity in the original US image, and σ^2 is the corresponding variance value in (4.5). $I_{k,f}(p_x, p_y)$ is the intensity of the US image after removing the noise using Wiener filter and ν^2 is the noise variance in the image in (4.6). The increase in the noise value in the high force values is

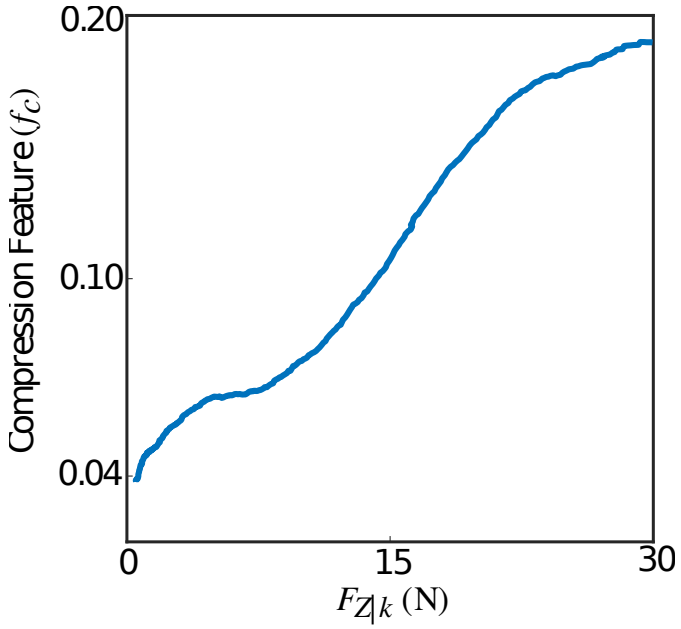

Figure 4.4: Compression feature with respect to measured force

due to the nature of speckle noise in ultrasound and interference of ultrasound signals inside the tissue. (4.7) finds the difference between US image I_k and filtered image $I_{k,f}$ to find the US image's noise. In (4.8), $\overline{I_n}$ is the average of noise in the image and σ_n is the corresponding standard deviation value. Figure 4.5 shows two images with high level (Figure 4.5a) and low level (Figure 4.5b) of noise. We have also shown in Figure 4.6, the variation of the noise feature f_n in the US image with respect to measured force $F_{Z|k}$.

4.2.2 Support Vector Machine (SVM)

The compression and noise features mentioned above will be used as an input to the SVM classifier (e.g, taking the output of the image feature calculation, (4.3) and (4.8), for I_k we then calculate the SVM score) and the correlation feature works as a gate. SVM classifier tries to find a line that separates two classes based on the features in feature space. SVM finds this line by optimizing a cost function based on the margin between two classes in feature space. There may be a need to increase the features' dimension to find this line in a higher dimensional space.

We trained SVM model with Gaussian kernels using our dataset and tested

(a) Ultrasound image with a high levels of noise

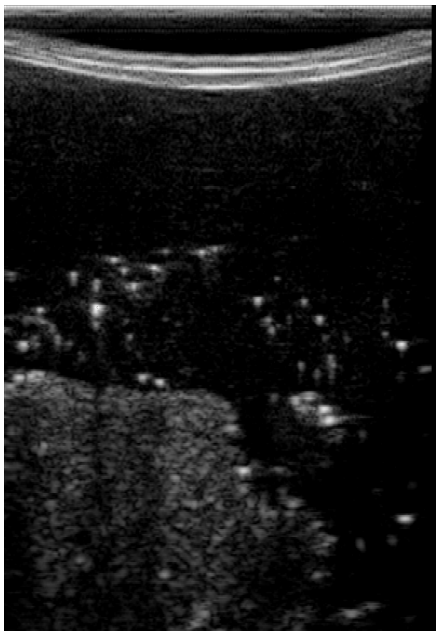

(b) Ultrasound image with a low levels of noise

Figure 4.5: Ultrasound images with high and low levels of noise

it using cross-validation. We used two different tissue phantoms to train and test the SVM, meaning we trained the SVM using one of the phantoms and tested it on the other phantom. The phantoms were biological porcine and bovine tissue. We trained the SVM using bovine phantom, and the trained SVM was tested on porcine tissue and vice versa. We will use the output of the SVM for robotic control.

We created an image database for training and testing the SVM. To create a database, we used a robot arm to scan bovine and porcine tissue phantoms by scanning multiple points on these tissues automatically by increasing force values at each point. The scanning procedure started from one side of the tissue and continued by dividing them to many points and increasing the US scanning force applied to the tissue from 1 N to 20 N with an increment of 0.25 N. The force increment was based on force control feedback in the robotic arm by increasing the tissue indentation until the force value reached the desired force. This procedure was just used for creating a bovine and

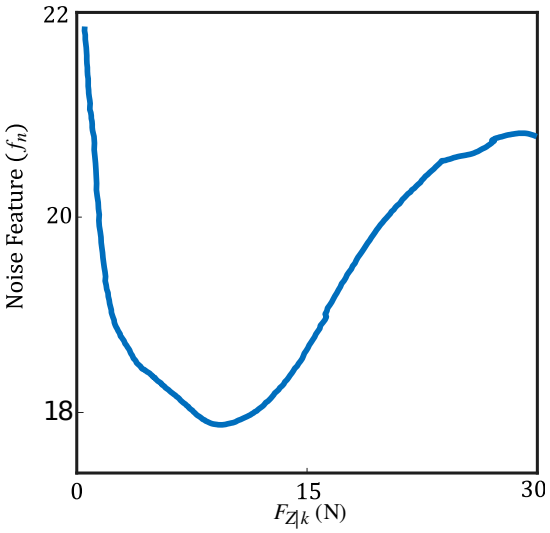

Figure 4.6: Noise feature with respect to measured force

porcine image database. The images captured at each point on the tissue and the forces' value were saved using a computer. A trained non-medical user then manually classified all images and a subset of 1000 images selected with 500 high-quality images and 500 low-quality images from the tissue phantoms' US images for different force values. The images were classified subjectively by the user, and the images were determined to be high quality if there is sufficient contact between tissue and the probe and tissue is visible without significant deformation within the US image. The variation of the pixel intensity in the frame with respect the background was also been considered for image classification. The SVM was trained using 800 images with equal probability weighting in each of the two classes. The trained SVM was tested on the remaining 200 images. After training, the SVM has reached an accuracy (a ratio of the number of correct labels to all labels) of 96% on our test database. Figure 4.7 shows the procedure of training SVM using biological porcine and bovine tissue.

The rule for updating the force's value based on the output of the image quality assessment algorithm is shown in (4.9) and (4.10). We have also shown a block diagram of the quality assessment algorithm in Figure 4.8.

$$V_{svm} = SVM(f_c, f_n); V_{svm} \in \{0, 1\} \tag{4.9}$$

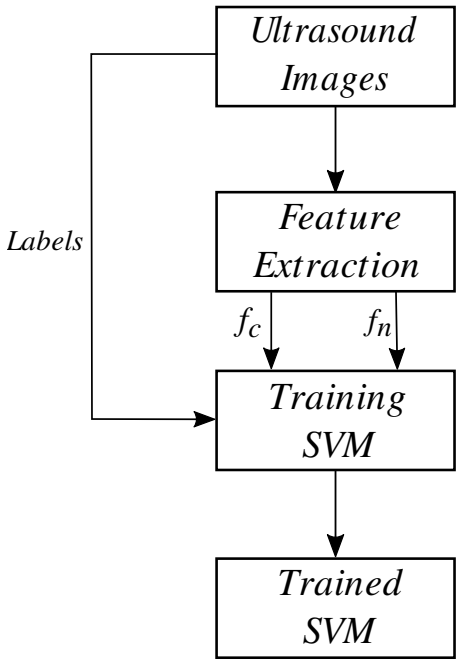

Figure 4.7: SVM training procedure

$$F_{Z|k+1} = F_{Z|k} + \delta F(1 - V_{svm}) \tag{4.10}$$

4.3 Robot Admittance Control

Our admittance controller in the x-y-z direction keeps the robot in the original x-y position and updates the z position based on the image quality assessment algorithm, as mentioned earlier. We transform the force sensor data into the base frame of the robot. Figure 4.1 shows the robot coordinate system during the experiments.

We use the output of the quality assessment algorithm in the loop controlling the force applied by the US probe to tissue. Figure 4.9 shows the control loop for the z-axis used during the experiments. The admittance model calculates desired position of the robot based on the input force. K_θ is the gain for calculating how much torque should be applied at joints. The control loop works on two different frequencies. Dash lines in Figure 4.9 represent image-quality feedback working on 30 Hz, and the solid lines represent robotic control working on 1 kHz. We reduced the sampling time of robotic control to 30 Hz

to avoid discrepancies during our experiment.

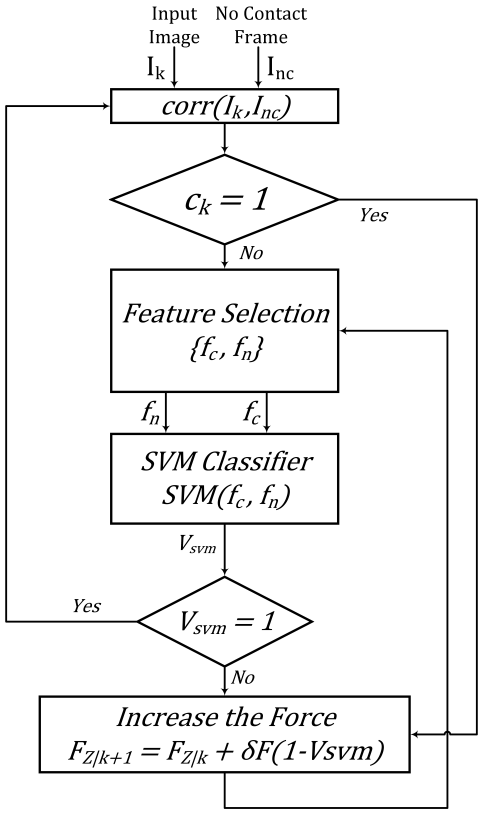

Figure 4.8: Quality assessment algorithm

The value of the force applied to the tissue in the z-direction is fed to the admittance controller. The transfer function describes the admittance model in (4.11). Where $X_k(s)$ is the desired Cartesian position in the robot base frame, and $F_k(s)$ is the force applied to the end effector in the robot base frame in the z-direction. $\mathbf{M}$ is the virtual mass matrix specified for the system. $\mathbf{B}$ and $\mathbf{K}$ represent specified damping and spring matrices, respectively. The matrices $\mathbf{M}$, $\mathbf{B}$ and $\mathbf{K}$ are shown in Section 4.4. The admittance model in the feedforward finds the desired position for the system, while the feedback impedance model calculates the robot's current position. We multiply the error by inverse jacobian J^{-1} and K_θ to find the error in joint space, and torque should be applied at joints.

$$H(s) = \frac{X_k(s)}{F_k(s)} = \frac{1}{\mathbf{M}s^2 + \mathbf{B}s + \mathbf{K}} \tag{4.11}$$

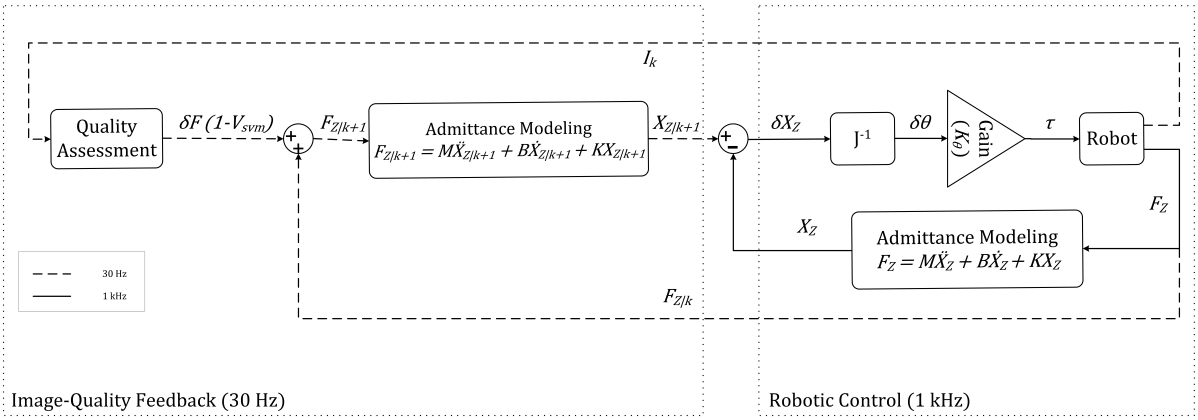

Figure 4.9: Robot control for the z axis

For the experimental setup and results, which will be covered in 4.4, We chose the values of **M**, **B** and **K** for the parameters of the admittance model, as shown in the following matrices. The matrix of **K** has only one non-zero parameter (in the z direction) that controls the US force applied to the tissue. The values of **M** and **K** are based on [50], and they were chosen empirically as a trade-off between sluggishness and control of the system. We calculated the value for **B** to have a critically damped response in the z-direction. The threshold values in our quality assessment algorithm were found empirically based on the SVM response in our US image database, these values are $t_{corr} = 0.7$ and $t_{comp} = 20$.

$$\mathbf{M} = \begin{bmatrix} 5.625 & 0 & 0 \\ 0 & 5.625 & 0 \\ 0 & 0 & 5.625 \end{bmatrix} kg$$

$$\mathbf{B} = \begin{bmatrix} 33.54 & 0 & 0 \\ 0 & 33.54 & 0 \\ 0 & 0 & 33.54 \end{bmatrix} \frac{N \cdot sec}{m}$$

$$\mathbf{K} = \begin{bmatrix} 0 & 0 & 0 \\ 0 & 0 & 0 \\ 0 & 0 & 50 \end{bmatrix} \frac{N}{m}$$

4.4 Experimental Setup and Results

In this study, an Axia80-M20 force-torque sensor (ATI Industrial Automation, Apex, NC, USA) was mounted on a Panda robotic arm (Franka Emika GmbH, Munich, Germany), which holds US probe (see Figure 4.1). We have used US machine for capturing images with an Epiphan DVI2USB3.0 (Epiphan Systems Inc, California, USA) for sending the image to the computer. The US machine used for the experiment was an Ultrasonix Touch with a 4DL14-5/38 Linear 4D transducer (Ultrasonix Corp, Richmond, BC, Canada). For this experiment, we only use the 2D functionality of the US probe. We used a tissue phantom made of plastisol as an artificial tissue for our experiment. The setup is shown in Figure 4.1.

The admittance controller was programmed and implemented in MATLAB 2019a (The Mathworks Inc, Natwick, MA, USA) and ran using Simulink on a PC running Ubuntu 16.04 LTS. The PC has an Intel Core i5-8400 running at 4.00 GHz. The communication between robot and computer was done over UDP, and the Epiphan was connected to the computer using a USB port.

To evaluate the image quality controller algorithm, we selected six spots on the surface of the plastisol tissue and ran the proposed method on those six locations. We then manually classified the acquired images and found the values of Structural Similarity Index Metric (SSIM) and Peak Signal to Noise Ratio (PSNR) between the output of our quality assessment algorithm and our manual subjective results. The calculation of SSIM is based on [63]. These values are reported in Table 4.1.

The experiments are designed to test the feasibility of incorporating our quality assessment algorithm into the control loop. The robot increases the force applied to the tissue by going down in the z-axis using an admittance controller. Figure 4.10 shows the output of the quality assessment algorithm and the subjective result by the human operator. Figure 4.10a is the output of the quality assessment algorithm in one specific position and Figure 4.10b is the output of the manual classification of the image in that specific position. This will show that our proposed method provides US images of high quality

Location	**SSIM**	**PSNR**
First Position	0.87	26.85
Second Position	0.76	20.60
Third Position	0.84	24.30
Fourth Position	0.88	28.16
Fifth Position	0.86	24.53
Sixth Position	0.82	22.54

Table 4.1: Similarity metrics' value between quality assessment algorithm and subjective classification

similar to those taken by a sonographer.

The values reported in Table 4.1 show the US image captured using our proposed image quality assessment method is similar to the result of manual classification. The similarity between the values of SSIM and PSNR in all six positions proves the generality of the proposed quality assessment method. Being as PSNR only compare the values of intensities without analyzing general features of the image like the shape of the organ inside the tissue. The SSIM finds the similarities between two images based on structural analysis. The values of SSIM are high for our experiment, which proves our algorithm performs very close to a human operator.

We evaluated the performance of the proposed method experimentally by recording the values of each feature and the output of SVM by controlling the force applied to the tissue. Figure 4.11 shows the average value of compression value with respect to the force applied to the tissue during the test experiment. The values reported in this figure, are the average compression feature values in six different spots on the surface of the tissue. The bar in each force value represents the variation of the compression feature at the corresponding force value at all six locations on the tissue. We also reported the same variation

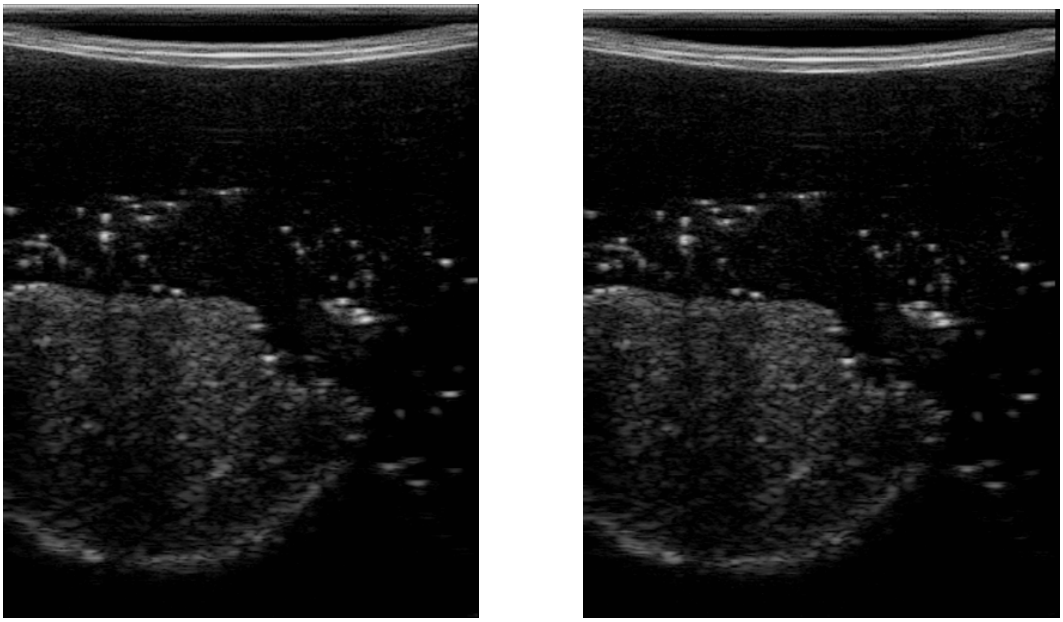

(a) Quality assessment output (b) Subjective result

Figure 4.10: Output of quality assessment algorithm and human subjective classification

for noise feature in Figure 4.12. Figure 4.13 shows the variation of SVM output during scanning of the tissue by increasing the force applied to it. The threshold value of t_{SVM} divides the graph to two separate classes in which the top part is associated with class of high-quality images and the bottom part is related to the low-quality images. These graphs prove the generality of our proposed method in different situations as the variation of each feature across the different levels of force was within the limited range in all six locations on the tissue.

The experiments conducted in this section shows us that the level of force applied to the tissue using the quality assessment algorithm is whitin a reasonable range, based on the results shown in Figures 4.11, 4.12 and 4.13. The general trend and variation of these features during scanning are consistent with respect to the applied force, which proves the generality of the proposed method. The output of the SVM shown in Figure 4.13 shows that the SVM classifier is able to give positive scores to high-quality images in the experiment while it gives negative values to the low-quality images. Figure 4.10 and Table 4.1 show us that the output of the quality assessment algorithm is very

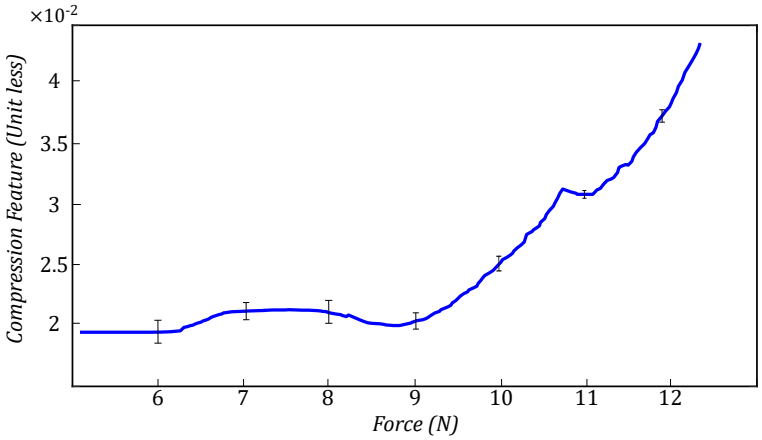

Figure 4.11: Variation of compression feature during the test experiment in all six spots on the surface of the tissue

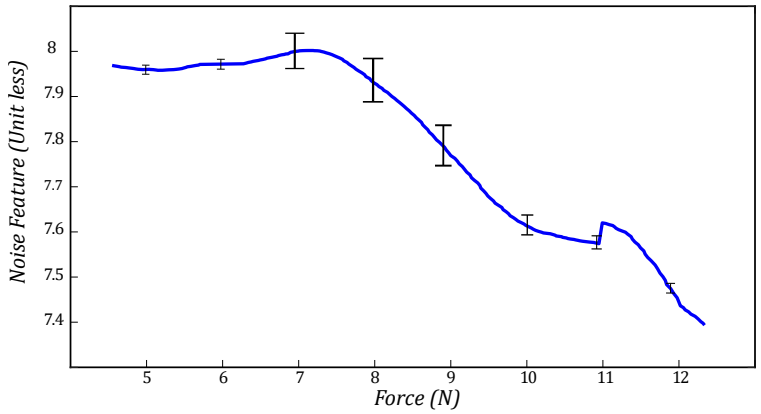

Figure 4.12: Variation of noise feature during the test experiment in all six spots on the surface of the tissue

close to the desire of the sonographer that all the values reported in Table 4.1 are whitin a reasonable range and the image acquired using image quality assessment algorithm and the subjective result are very close to each other in Figure 4.10.

4.5 Conclusion

This chapter has presented US image quality assessment algorithm used for robotic control of US scanning. Our proposed quality assessment algorithm uses feature extraction and a SVM classifier to assess the acquired images'

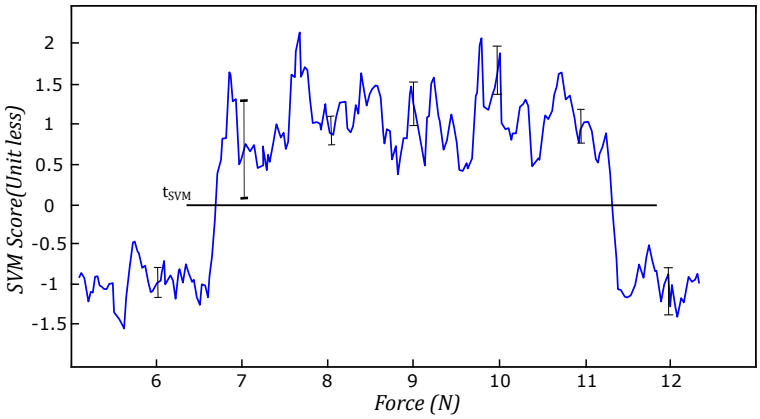

Figure 4.13: Variation of SVM during the test experiment in all six spots on the surface of the tissue

quality. The algorithm estimates the US image's quality based on correlation, compression, and noise features. These features are input into a SVM classifier to determine an image is of high quality or low quality. The algorithm was used as a part of the real-time control loop in the robotic US image scanning system. The user is able to put the US probe at a specific location on the tissue, and the algorithm will modulate the US scanning force applied to the tissue. An admittance controller was used internally to modulate the force. We evaluated the performance of the proposed system using different quality assessment metrics, showing close agreement between manual subjective assessment of the captured US image quality and the quality estimation from our algorithm.

This system is designed to enable isolation between patients and sonographers during the COVID-19 pandemic. In the future, we can control the US probe's orientation in an autonomous manner to enable six degrees of freedom of the US probe during scanning. We can also incorporate the quality assessment algorithm into a teleoperation system to enable remote control of a US scanning robot. Here, the user can remotely move the robot to the desired location, with the algorithm appropriately adjusting the US scanning force automatically.

Chapter 5

Safe Motion Planning for Lower-limb Exoskeleton[1]

5.1 Introduction

Deep learning has seen successful applications in various medical domains, leveraging the abundance of available data and data-driven system development approaches. However, quality issues in current deep learning-based methods raise significant concerns, particularly in safety-critical medical applications [5], which require high safety standards. Medical robots, in particular, are safety-critical systems, and when data-driven Artificial Intelligence (AI) is integrated as the decision-maker within the robot control system, thorough safety analysis becomes imperative [47]. Data-driven AI models, such as deep neural networks, learn decision logic based on training data and are expected to perform well on unseen data following a similar distribution. Nonetheless, deep learning lacks statistical guarantees for reliable performance on a wide range of input scenarios and struggles with handling data outside the training distribution [72]. This limitation can be critical, as AI-enabled medical robots rely on imagers and sensors feeding a DNN for decision-making. To address safety concerns and avoid uncertain predictions with potential catastrophic consequences, it becomes essential to analyze when input data falls outside the deep neural network's decision boundary. This motivates our proposal for integrating an uncertainty assessment technique into the control loop of med-

[1]A version of this chapter has been published as Uncertainty-aware Safe Adaptable Motion Planning of Lower-limb Exoskeletons Using Random Forest Regression

ical robots, continuously monitoring DNN actions and decisions to enhance safety in human-robot interactions.

In this chapter, we tackle the challenge of using uncertainty in deep learning decision-makers within the robot's control loop while ensuring real-time performance, an aspect not previously explored. To achieve this, we adopt random forest regression (RFR) to predict the passive dynamics of the human-exoskeleton system, considering position, velocity, and acceleration of six joints as inputs. This estimation of human-exoskeleton interaction torque informs and updates motion planning, adjusting the exoskeleton's motion based on the user's applied torques. Our contribution involves incorporating uncertainty estimation in the adaptable Central Pattern Generator (CPG) dynamics for gait motion planning, aiming to enhance safety in human-robot interaction. Specifically, we utilize Kullback-Leibler (KL) divergence between training labels and predictions to measure RFR's uncertainty. Additionally, we employ Mahalanobis distance to determine the distance between the current input and training distributions, acting as the out-of-distribution (OOD) detection part of our proposed technique. It is important to note that the uncertainty analysis technique we propose is a framework that considers data distribution and is agnostic to the specific learning technique used within the framework.

The rest of this chapter is organized as follows. First, in Section 5.2, we introduce the proposed uncertainty analysis technique and details of modified CPG equations with the consideration of prediction uncertainty. Then, in Section 5.3, we demonstrate the experimental result of the proposed method, followed by the concluding remarks in Section 5.4.

5.2 Methodology[2]

This section introduces the background and mathematical formulations of the proposed uncertainty-aware exoskeleton control technique. This strategy adjusts the gains in the CPG based on the uncertainty of random forest predic-

[2]The list of variables used in this section and their definitions are available in the Appendix

tions to give the exoskeleton the ability to have safe interactions with human users. The overview of the proposed technique is summarized in Figure 5.1. Here, τ_{motor} is the total torque measured by exoskeleton torque sensors, τ_{exo} is the torque applied to the exoskeleton's joint by joint-level position controller, and τ_h is the human torque vector.

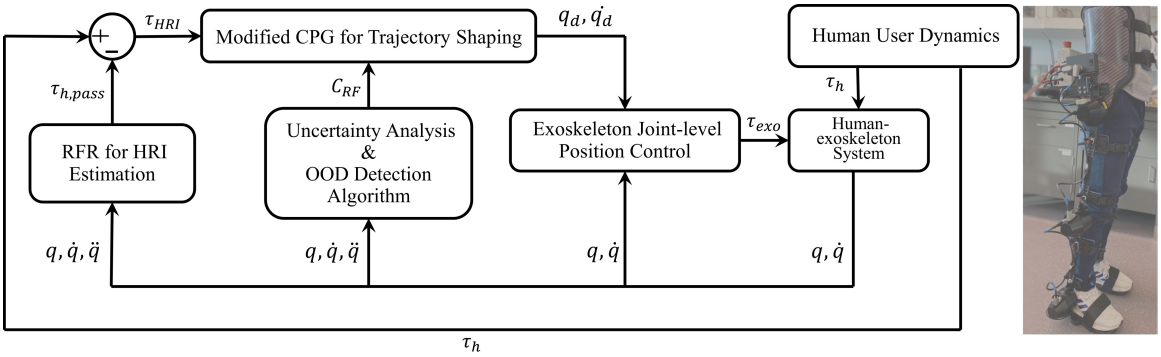

Figure 5.1: Overview of proposed uncertainty-aware exoskeleton control method.

5.2.1 Random Forest Regressor Method for HRI Estimation

The non-linear dynamics of multi-DOF lower-limb exoskeleton interacting with the human user is

$$M_q(q)\ddot{q} + C_q(q)\dot{q} + G_q(q) = \tau_{HRI} + \tau_{motor} + \tau_{h,pass}. \tag{5.1}$$

Here, q is the exoskeleton's joint positions vector, $M_q(q)$ is the inertia matrix, $C_q(q)$ is the Coriolis, centrifugal and damping term, and $G_q(q)$ is the gravitational torques. The torque values on the right side of (5.1) are exoskeleton motor torque (τ_{motor}), human-robot interaction (HRI) torque (τ_{HRI}), and passive dynamics of human exoskeleton system ($\tau_{h,pass}$). The passive dynamics of the human exoskeleton system is defined as the exoskeleton joint torques required to drive a user in the absence of any interaction between the human and the exoskeleton. Given these passive torque values, the active human-robot interaction torque can be calculated as the difference between measured joint torque applied by human (τ_h) and estimated passive torque. Our proposed

method uses ensemble decision trees in the form of a random forest regression (RFR) for estimating the passive torque ($\tau_{h,pass}$) that is used for estimating HRI torque (τ_{HRI}) using

$$\tau_{HRI} = \tau_h - \tau_{h,pass}. \tag{5.2}$$

τ_{HRI} calculated in (5.2) is used to calculate the energy transferred between the human user and exoskeleton. The frequency and amplitude of the desired trajectory will be affected by the energy in walking with an exoskeleton. The mathematical details are given in Section 5.2.2.

Random forests are multiple decision trees with voting schemes at the end of these trees for making predictions. Decision trees have proven to have a good performance for regression problems and are easy to be trained on commodity hardware [51], [53]. The complexity and the performance of the regression algorithm are essential considerations in our application under the context of a medical robot. The performance is also critical as the decision coming from RFR affects the physical human-robot interaction (pHRI). Figure 5.2 shows the structure of the model that has been developed for estimating the passive torque of the human ($\tau_{h,pass}$).

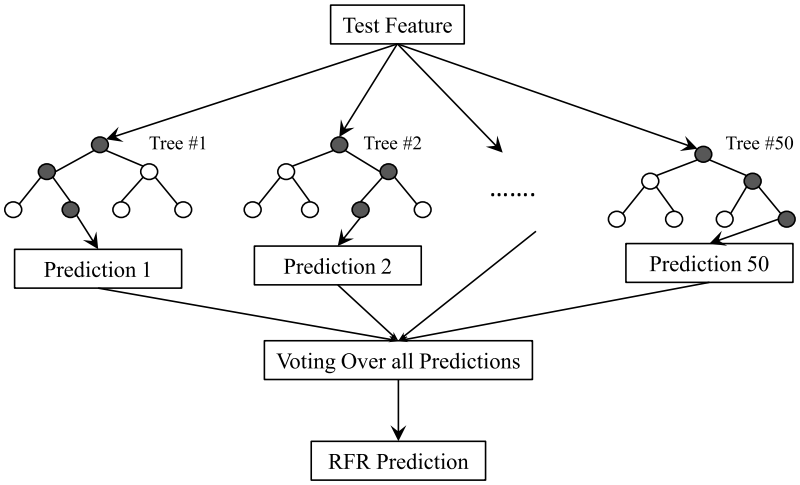

Figure 5.2: Random forest model for human passive torque estimation $\tau_{h,pass}$

In this experiment, we asked a human user to walk with an exoskeleton over the ground in several training data collection trials. We used CPGs with different walking speeds for trajectory shaping during these trials. Each exoskeleton

joint's position, velocity, acceleration and corresponding motor torques have been saved. The user was asked to comply with the exoskeleton-imposed motion and not apply any force to the exoskeleton so that the torque of each joint equals the passive torque. We changed the velocity of the exoskeleton walking for training the random forest. The position, velocity and acceleration of the exoskeleton's joints $(q, \dot{q}, \ddot{q})$ are the input to the random forest model and the estimated passive torques of each joint $(\tau_{h,pass})$ is the output. Applying torques to the joint of the exoskeleton will result in faster motions. Hence, τ_{HRI}, which has a direct relation to the energy transferred between the user and exoskeleton, is used in the modified adaptable CPGs algorithm for shaping the trajectory of the exoskeleton along with its uncertainty.

5.2.2 Modified Adaptable CPG for Trajectory Shaping

Modified adaptable CPG dynamics are used for designing gait trajectories based on HRI torque. The HRI torque (τ_{HRI}) is used for calculating the energy transferred between the user and exoskeleton. This is inspired by the method in [39], [59]. We calculate the energy of each joint i by using the HRI torque and the velocity of each joint as

$$E_i(t) = \int_0^t \tau_{HRI_i}(t)\dot{q}_i(t). \tag{5.3}$$

Here, $\tau_{HRI_i}(t)$ is calculated using (5.2) for each joint and $\dot{q}_i(t)$ is the velocity of each joint coming from the exoskeleton sensors $(i = 1, ..., n)$. The modified adaptable CPG dynamics for the desired joint trajectory generation based on the amplitude and the frequency update are proposed as

$$\begin{aligned}
\dot{\phi}_i(t) &= f(t) + \sum_{j=1}^{N_i} \nu_{ij} \sin\left(\phi_i(t) - \phi_j(t) - \psi_{ij}\right) \\
\ddot{f}(t) &= \alpha_f\left(\frac{\alpha_f}{4}\left(F + C_{RF}(f_{test}) \sum_{k=1}^{n} \lambda_k E_k - f(t)\right) - \dot{f}(t)\right) \\
\ddot{a}(t) &= \alpha_a\left(\frac{\alpha_a}{4}\left(A + C_{RF}(f_{test}) \sum_{k=1}^{n} \eta_k E_k - a(t)\right) - \dot{a}(t)\right).
\end{aligned} \tag{5.4}$$

Here, N_i is the number of adjacent joints to the joint i. $a(t)$ is the amplitude of the movement, and $f(t)$ is the frequency of the movement. α_f and α_a are

constant parameters. λ_k and η_k are constant gains for updating the frequency and amplitude of the gait cycles, based on the injected pHRI energy E_k defined in (5.3). A change in frequency will result in changes in walking speed, while a change in amplitude will result in changes in the walking step length of the user with the exoskeleton. In the above, we have modified the adaptable CPG dynamic proposed in [39], [59] by adding $C_{RF}(f_{test})$ to the energy term in the frequency and amplitude dynamic formula. Here $C_{RF}(f_{test})$ is the uncertainty in the estimation of passive torque using RFR and will be explained in Section 5.2.3. Adding $C_{RF}(f_{test})$ to (5.4) enables the algorithm to scale the effect of the pHRI energy in the CPG gait trajectory update. For instance, if the input feature is far from the distribution of the training data, the distance value will be high. Then this technique is able to reduce the effect of the energy term in (5.4) by using $C_{RF}(f_{test})$ found in (5.8).

We now can formulate the desired trajectory of joint i using (5.4) and Fourier series as

$$q_{d_i}(t) = a(t)(c_{i_0} + \sum_{j=1}^{N_i}(c_{i_j}\cos j\phi_i(t) + d_{i_j}\sin j\phi_i(t))). \tag{5.5}$$

Here, c_{i_j} and d_{i_j} are the Fourier series coefficients for each joint's trajectory. The trajectory calculated in (5.5) considers the uncertainty of the prediction in real-time using (5.8) and (5.4). The proposed adaptable CPG can be used in any other motion planning approach for exoskeletons in a similar manner. We did it for CPGs as one example of motion planning methods for the lower-limb exoskeleton.

5.2.3 Uncertainty Analysis & OOD Detection

Our proposed uncertainty analysis technique considers both the training and run-time prediction phase for determining the uncertainty of the prediction. The similarity between training labels and model predictions during training is a measure that can be used to assess the model's reliability for an input that falls inside the training distribution. We use Kullback-Leibler (KL) divergence as a similarity measure in this regard. Our proposed technique finds

the Mahalanobis distance between the input feature and training data distribution during the test phase to check how far the test feature is from the training data for updating uncertainty values. This mechanism refines the initial uncertainty measure found using KL divergence for the test sample in real time. Using Mahalanobis distance for OOD detection is inspired by the method proposed in [32]. The overview of the proposed uncertainty analysis and OOD detection technique is shown in Figure 5.3. O_{train}, L_{train} and F_{train} are predictions of the training set, labels of the training set and input training features, respectively. These data are used for calculating KL divergence.

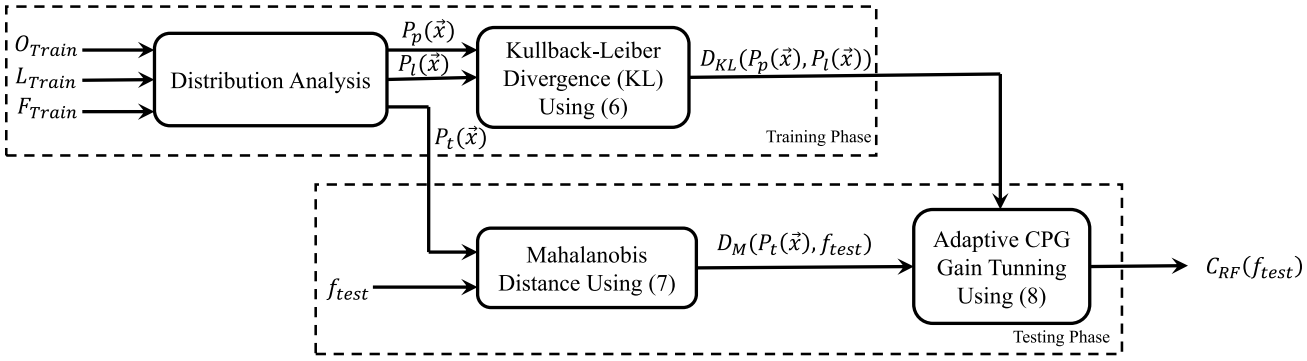

Figure 5.3: Overview of proposed uncertainty analysis and OOD detection technique.

KL Divergence as Similarity Measure

The Kullback-Leibler (KL) divergence, $D_{KL}(P_l(\overrightarrow{x}), P_p(\overrightarrow{x}))$ is a statistical measure of how a distribution $P_p(\overrightarrow{x})$ is similar to a reference distribution $P_l(\overrightarrow{x})$. The KL divergence between two discrete distributions $P_l(\overrightarrow{x})$ and $P_p(\overrightarrow{x})$ is calculated as

$$D_{KL}(P_l(\overrightarrow{x}), P_p(\overrightarrow{x})) = \sum_{\overrightarrow{x} \in \chi} P_l(\overrightarrow{x}) \log \frac{P_l(\overrightarrow{x})}{P_p(\overrightarrow{x})}. \tag{5.6}$$

Here, $P_l(\overrightarrow{x})$ and $P_p(\overrightarrow{x})$ are the distributions of the labels and predictions on the training set, respectively. χ is the probability space where distributions are defined. The mathematical details of the distribution analysis for KL divergence is demonstrated in Section A (Appendix).

Mahalanobis Distance for OOD Detection

Mahalanobis distance is a statistical measure of the distance between a point and a distribution. Assume a vector $\overrightarrow{v} = [v_i]_{i=1}^{n}$ and a distribution P with mean value of $\overrightarrow{\mu}$ and covariance matrix (Σ). The Mahalanobis distance between vector $\overrightarrow{v}$ and distribution P is

$$D_M(P, \overrightarrow{v}) = \sqrt{(\overrightarrow{v} - \overrightarrow{\mu})^T \Sigma^{-1} (\overrightarrow{x} - \overrightarrow{\mu})}. \tag{5.7}$$

The covariance matrix Σ is a positive definite matrix; hence its inverse exists and is also positive definite, and the root square is shown in (5.7) always has a real value.

In the proposed method, we use (5.7) to check how far input feature (f_{test}) is to the distribution of the training set ($P_t(\overrightarrow{x})$) for OOD detection. We calculate the histograms of training data, mean value $\overrightarrow{\mu_f}$ and covariance matrix Σ_f. Then we use (5.7) to find the distance value ($D_M(P_t(\overrightarrow{x}), f_{test})$). The distance found using (5.7) refines the initial uncertainty estimation obtained using (5.6) in real-time for the test sample. The resulting Mahalanobis distance is used in our proposed adaptable CPGs gain tuning technique described in Section 5.2.3.

Adaptable CPGs Gain Tuning Technique

Our proposed adaptable gain tuning algorithm should have the ability to account for the effect of uncertainty in the CPGs trajectory planning based on the distance between input feature and training distribution. We propose

$$C_{RF}(f_{test}) = \begin{cases} D_{KL}(P_l(\overrightarrow{x}), P_p(\overrightarrow{x})) \times D, & \text{if } D < 1 \\ 0, & \text{if } D \geq 1 \end{cases} \tag{5.8}$$

as the uncertainty input to be fed into the CPGs for controlling human-robot interaction during task execution. Here, C is a constant value (in the range of 60 to 80, which has been found empirically). $D \triangleq |1 - \frac{D_M(P_t(\overrightarrow{x}), f_{test})}{C}|$, and $D_{KL}(P_l(\overrightarrow{x}), P_p(\overrightarrow{x}))$ and $D_M(P_t(\overrightarrow{x}), f_{test})$ are from (5.6) and (5.7). The summarized version of the proposed uncertainty technique for adaptable CPG gain tuning is shown in Algorithm 2. This is important to note that the

proposed method only changes the coefficients of some terms in 2nd-order ordinary differential equations (ODEs) shown in (5.5) at a 20Hz rate. The ODEs will be numerically solved at a higher rate, so in practice, we see only a smooth and continuous gradual transition. The mathematical explanation of the effect of uncertainty in the CPG algorithm is demonstrated in Section 5.2.2.

Algorithm 2 Proposed Adaptable CPG Gain Tuning

Require: Training feature distribution ($P_t(\overrightarrow{x})$), Training label distribution ($P_l(\overrightarrow{x})$), Random forest prediction for training set distribution ($P_p(\overrightarrow{x})$), Gain constant (C), Training data distribution $\overrightarrow{\mu_{P_t}}$, KL divergence between predictions and labels $D_{KL}(P_l(\overrightarrow{x}), P_p(\overrightarrow{x}))$

1: **for** each f_{test} **do**
2: Find $D_M(P_t(\overrightarrow{x}), f_{test})$ using (5.7)
3: Find $C_{RF}(f_{test})$ using (5.8)
4: Update CPG equations and calculate amplitude and frequency of the trajectory using (5.4) and find $C_{RF}(f_{test})$ using (5.8)
5: **end for**

5.3 Results and Discussion

As a showcase of the proposed framework, an exoskeleton was utilized in this chapter. The exoskeleton is operated by a human user who applies force to its joints, resulting in additional torques on the torque sensors. If the interaction torque does not align with the distribution of data on which the model was trained, an unsafe situation may arise. This would result in the model making inaccurate decisions and potentially endangering the user who interacts with the exoskeleton.

We have tested our proposed method on the ExoH3 (Technaid S.L.) exoskeleton, Madrid, Spain. A non-disabled human user with a height of 173 cm and weight of 67 kg wore the exoskeleton while also using crutches as shown in Figure 5.4. The trajectory of the walking has been saved and Fourier series analysis was conducted on the acquired trajectory to obtain a minimum number of series and the best coefficients. Eight terms of the Fourier series were sufficient and attained coefficients of the hip, knee and ankle motions are

listed in Table 5.1. Additionally, parameters and initial values of the CPG dynamics for hip, knee and ankle joints of both legs are listed in Table 5.2.

Figure 5.4: Experimental setup with the human user.

This experiment was planned for two scenarios with and without uncertainty analysis to evaluate the proposed technique's performance in the exoskeleton's control loop. Real-time Desktop MATLAB/Simulink was employed for receiving the sensory data and sending the control commands to the exoskeleton. The sampling frequency was 20 Hz. For this, the exoskeleton was connected to a laptop with a CAN interface (Vector VN1610) running on a Core i7 CPU with 16 GB RAM. We implemented the RFR model on a different PC using Python programming language and scikit-learn machine learning library [49]. We used the UDP communication protocol for sending and receiving data between the PC and the laptop.

We trained the RFR model for learning the passive human-exoskeleton dynamics using our training dataset. The same user was asked to wear the exoskeleton and walk on the ground without interacting with the exoskeleton. The authors are aware that it is hard to make human-robot interaction zero during the experiment. The HRI torque has two parts, intentional and unintentional torque. The intentional torque is used in the adaptable CPG for

	Hip initial motion	Knee initial motion	Ankle initial motion
Coefficients of Fourier series	$a_0 = 5.057$, $a_1 = 6.222$, $a_2 = 0.521$, $a_3 = 0.052$, $a_4 = 0.456$, $a_5 = 0.032$, $a_6 = 0.186$, $a_7 = -0.06$, $a_8 = 0.014$, $b_1 = 19.24$, $b_2 = 5.028$, $b_3 = 1.272$, $b_4 = -0.01$, $b_5 = -0.49$, $b_6 = 0.131$, $b_7 = -0.01$, $b_8 = 0.073$,	$a_0 = 12.28$, $a_1 = 19.88$, $a_2 = 11.76$, $a_3 = 7.327$, $a_4 = 4.888$, $a_5 = 2.369$, $a_6 = 0.957$, $a_7 = -0.38$, $a_8 = 0.180$, $b_1 = -0.95$, $b_2 = -0.37$, $b_3 = 0.707$, $b_4 = 1.083$, $b_5 = 1.231$, $b_6 = 0.962$, $b_7 = 0.405$, $b_8 = 0.115$,	$a_0 = 6.842$, $a_1 = -6.46$, $a_2 = -2.77$, $a_3 = -0.35$, $a_4 = 0.369$, $a_5 = 0.590$, $a_6 = 0.552$, $a_7 = -0.28$, $a_8 = 0.165$, $b_1 = -4.03$, $b_2 = 4.996$, $b_3 = 5.156$, $b_4 = 1.475$, $b_5 = 0.876$, $b_6 = 0.388$, $b_7 = 0.242$, $b_8 = -0.004$,

Table 5.1: Coefficients of the Fourier series (5.5) for the hip, knee and ankle initial motions based on the analysis of normal gait trajectories

	Hip, knee and ankle CPGs' parameters
Dynamic parameter values	$\nu_{h-h} = 0.5$, $\nu_{h-k} = 0.5$, $\nu_{k-h} = 0.5$, $\nu_{a-k} = 0.5$, $\nu_{k-a} = 0.5$, $\nu_{a-a} = 0.5$, $\alpha_f = 15\pi$, $\alpha_a = 15\pi$, $\psi = 0.7$, $\lambda = 0.3$, $\eta = 0.3$, $F = 0.35\pi$, $A = 1$
Initial values	$\phi_{right}(0) = 2\ rad$, $\phi_{left}(0) = 2 + \pi\ rad$, $f(0) = 0.1\pi\ rad/s$, $a(0) = 0.1\pi\ rad$

Table 5.2: Parameter and initial values of CPG dynamics (5.4) for the hip, knee and ankle joints

trajectory shaping. The average value of the torque was subtracted from the experimental torque to make sure that unintentional torque is not included in the experiment. The kinematic data (position, velocity and acceleration) and the torque values of each exoskeleton joint were recorded during this walking. 80% of the data was used to train the model, and the rest was used for testing. After training the model using 5-fold cross-validation, we reached the average mean absolute error (MAE) value of $0.014(N.m)$ on our test set.

In the first scenario, the user walked with the exoskeleton while interacting with it, but the uncertainty analysis algorithm was turned off. In this scenario, we revised the CPG algorithm to create the desired trajectory for the exoskeleton joints by considering the energy transferred between the user and the exoskeleton. In the second scenario, while the CPG was revised according to the user-exoskeleton energy transfer, we also turned the uncertainty analysis technique on. We evaluated its performance in detecting unsafe decisions and changing CPG's gains when the exoskeleton is making a potentially unsafe decision and taking potentially unsafe action in two user trials. In this way, we evaluated and compared the performance of the uncertainty analysis technique by monitoring the amplitude and frequency of the trajectory created by the CPG with and without the uncertainty gain. We present the experimental results for the first scenario in the time interval between 20 (sec) and 80 (sec) as it is a time interval during which the user interacts with the exoskeleton. The time interval for the second scenario is between 50 (sec) and 250 (sec) as in this time interval, the user interacts with the exoskeleton and applies additional torques to the exoskeleton's joint.

5.3.1 Scenario one: CPG without Uncertainty Estimation Technique

We used eight terms of typical human gait's hip, knee and ankle motions Fourier coefficients for calculating CPGs' gait trajectory. The walking data were acquired during our experiment to make a training dataset. During the experiment, first, the CPG dynamics calculates the amplitude and frequency of the trajectory using (5.4) with $C_{RF}(f_{test}) = 1$. Then, the desired trajectory

is calculated in (5.5) using Fourier series coefficients.

A human user wore the exoskeleton as shown in Figure 5.4. We evaluated the position control algorithm's performance by comparing the exoskeleton points desired and current trajectories. This result is shown for the left and right knees in Figure 5.5. Figure 5.5 shows that the exoskeleton is able to follow the desired trajectory created by the CPG dynamics as the user interacts with it.

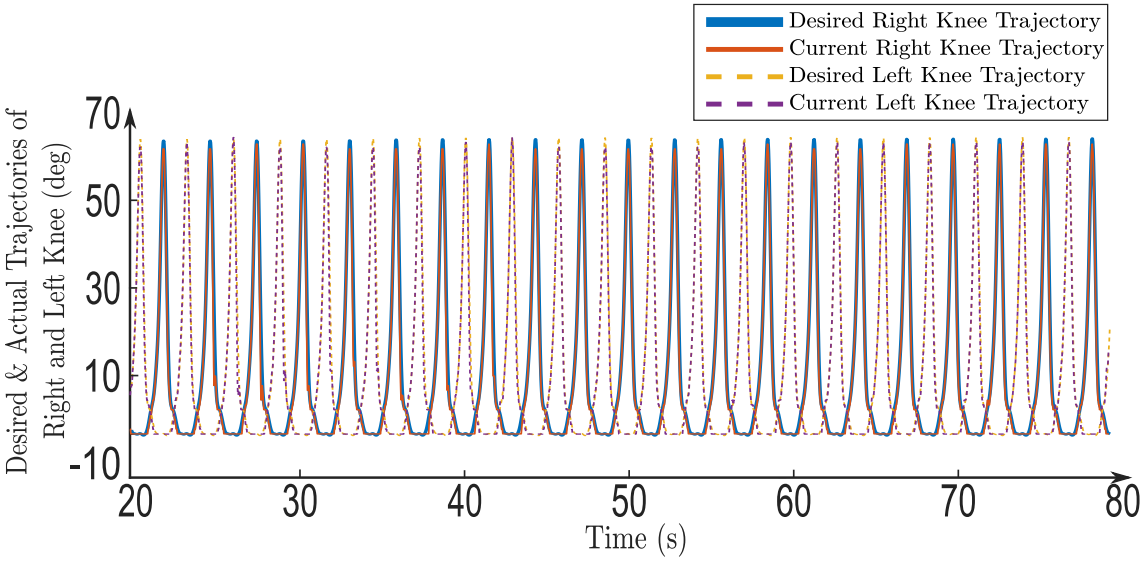

Figure 5.5: Desired and current trajectories of the right and left knee joints of the exoskeleton.

Next, the user applies active torques on different joints of the exoskeleton to analyze the CPGs' performance in changing the frequency and amplitude of the motions based on the energy transferred between the user and the exoskeleton. Figure 5.6a shows the total energy transferred between the user and the exoskeleton during the experiment. Figure 5.6b and Figure 5.6c show the amplitude and frequency of the desired trajectory created by CPGs following this energy transformation.

The experimental results in Figure 5.6 show that CPGs is able to change the desired trajectory of the robot as the user applies active torque to the robot's joints. This is implied in the spikes of Figure 5.6b and Figure 5.6c that happen when the user adds active torque to the system, shown in Figure 5.6a.

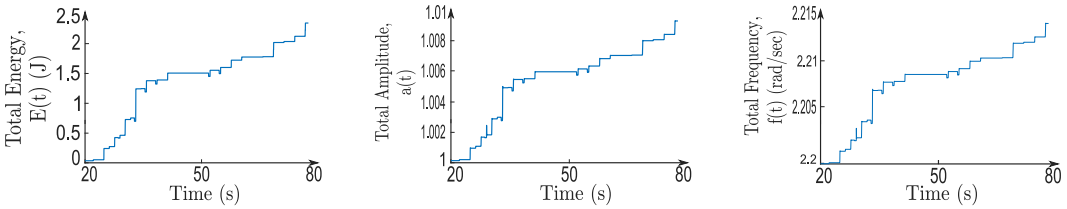

(a) Energy transferred between user and exoskeleton

(b) Amplitude of the desired trajectory calculated by CPGs

(c) Frequency of the desired trajectory calculated by CPGs

Figure 5.6: Performance of CPGs in designing trajectory based on energy transferred between user and exoskeleton

5.3.2 Scenario Two: Uncertainty Estimation Technique Performance Analysis

The performance of the proposed uncertainty analysis technique experimented with decisions from exoskeletons that may be unsafe for human users. This may result from irregular changes in the velocity of the exoskeleton during usage. As mentioned earlier, the training data was collected for walking on the ground with no interaction between the user and the exoskeleton. If the situation changes, the user may apply irregular torque to the joints of the exoskeleton, and CPG may interpret it as a speed-up request from the user. This can be an unsafe decision, and the uncertainty technique should detect it as OOD and stop the exoskeleton from speeding up. We tried to simulate this situation for the exoskeleton during our experiment in two separate user trials to evaluate the performance of the proposed uncertainty analysis technique. During our first user trial, we analyzed the performance of Mahalanobis distance and the thresholding algorithm in detecting unsafe actions. The proposed uncertainty analysis technique monitored the distance between the coming features and training set to inform the exoskeleton when an unsafe situation happens. The Mahalanobis distance between a test sample and the training set is a criterion for the proposed OOD detection algorithm. The distance between test features and training set before (Figure 5.7a) and after thresholding (Figure 5.7b) are shown in Figure 5.7.

The uncertainty detection technique should detect unsafe decisions of the

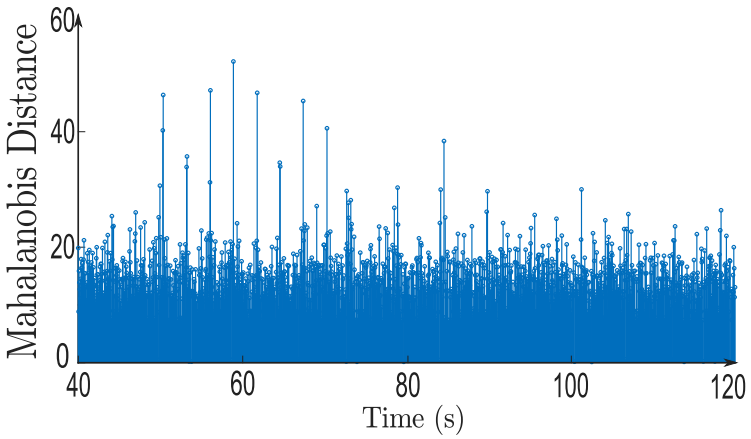

(a) Original values of Mahalanobis distance between test features and training set

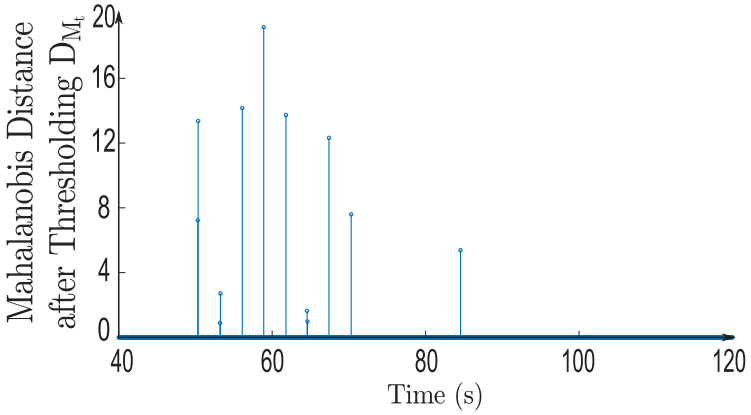

(b) Mahalanobis distance between test features and training set after thresholding.

Figure 5.7: Mahalanobis distance between test features and training set (5.7a) before and (5.7b) after thresholding for user trial #1.

exoskeleton and apply appropriate gains to CPG dynamics to modify its trajectory. The performance of the proposed uncertainty detection technique is shown in Figure 5.7b. During our first user trials, the distance between input features and the training set jumps when the user applies excessive torques to the exoskeleton, which results in an unsafe decision from the RFR. This situation is simulated in the experiment by asking the user to resist the changes in the trajectory coming from CPG. These jumps were exactly when we asked the user to start applying additional torques to the joint of the exoskeleton. We used two threshold values to keep jumps in Figure 5.7a and discard the rest. th_{up} and th_{down} are two threshold values that isolate unsafe actions of

the user using

$$D_{M_t}(f_{test}) = \begin{cases} S, & \text{if } S < th_{down} \\ 0, & \text{if } th_{up} > S > th_{down} \\ S, & \text{if } S > th_{up}. \end{cases} \tag{5.9}$$

Here, $S \triangleq D_M(f_{test}) - D_{offset}$ and we chose $th_{down} = -20$ and $th_{up} = 25$ to make sure that the thresholding method only selects unsafe actions and discards smooth interactions between the user and exoskeleton. We found these thresholds experimentally by walking with exoskeleton. The value of offset is $D_{offset} = 15$. The results shown in Figure 5.7b present a corresponding peak that can be considered as the level of uncertainty in our test feature.

Our proposed adaptable CPG gain tuning technique should limit the trajectory's amplitude and frequency growth whenever the user applies excessive torques to exoskeleton joints, which is caused an unsafe decision from exoskeleton. Furthermore, the gain value should be tuned based on the level of the uncertainty coming from the Mahalanobis distance of the test feature and training set using (5.8) and (5.7). We investigated the performance of our proposed adaptable CPG gain tuning during our second user trial. For this purpose, we first need to check whether our algorithm is real-time or not. Figure 5.8 shows the real-time features of our proposed method as an adaptable CPG gain tuning algorithm is triggered whenever the distance exceeds the tolerance interval. This is shown with lines from the top figure to the bottom figure in Figure 5.8. Figure 5.8 shows that our proposed method is able to detect unsafe decision from the kinematic data of the robot in real time, which make it applicable to real-time applications like robotic trajectory shaping.

Secondly, we monitored the amplitude and frequency of the trajectory generated by CPG during user trial # 2. The results are reported in Figure 5.9. The frequency and amplitude shown in Figure 5.9b and Figure 5.9a indicate that our proposed uncertainty algorithm is able to detect irregular actions and control the trajectory generated by CPG. The behaviour of the proposed method can be seen in Figure 5.9 as the blue trajectory, which is an output of the proposed algorithm, cancels the effect of unsafe actions in the trajectory generated by CPG (the blue line does not follow the orange line in the unsafe

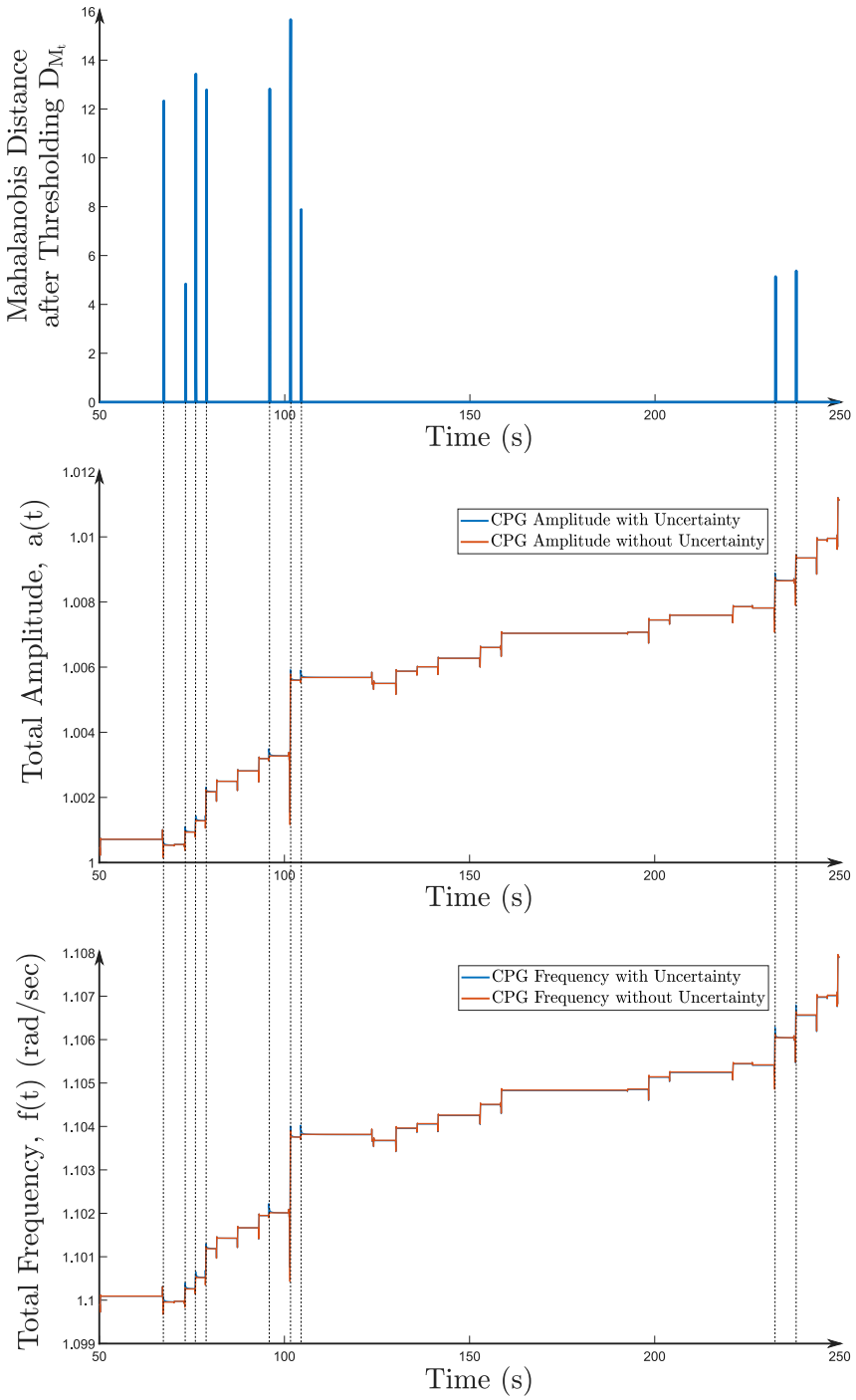

Figure 5.8: Analyzing real-time performance of proposed method in user trial # 2.

situations). The proposed method detects irregular jumps, decreases the trajectory's amplitude and frequency, and smoothly converges to the corresponding value (the blue line was shown with the thicker font for demonstration

purposes. In the actual result, the two lines are exactly fit to each other). This decrease and smooth convergence in the frequency and amplitude of the trajectory will vanish the effect of unsafe action on the user. Furthermore, a decrease in frequency will control the speed of the exoskeleton. A decrease in the amplitude will control the gait of the trajectory generated by CPG to enhance the safety of human-robot interaction.

5.4 Conclusion and Future Works

Deep learning has been applied in many medical applications. However, the safety and security concerns of using it in the control loop of medical robots have not been thoroughly investigated, which is a safety-critical application of deep learning. In this chapter, we proposed a method that can evaluate the uncertainty of the deep learning algorithm in real-time and use this uncertainty measure in the control loop of the robot to inform the system whenever the situation is unsafe for the user. Our proposed method finds the training features and label distributions during the training phase. When the training phase ends, the proposed method finds the distribution of the predictions when the training features feed into the model. The Kullback-Leibler (KL) divergence between predictions and labels is the initial uncertainty of the model. The uncertainty of the prediction for the input feature is updated based on the Mahalanobis distance of the test feature from the training distribution. The calculated uncertainty will update the effect of energy transferred between the user and the robot in the CPGs dynamics. This chapter used a random forest regression to estimate the human robot's passive torque.

The proposed method has been tested in the control loop of the ExoH3 (Technaid S.L.) exoskeleton with six degrees of freedom. The experiments were conducted in two scenarios. In the first scenario, we asked the user to walk with the exoskeleton and apply active torque to its joints to revise the CPG dynamics. In the second scenario, we evaluated the performance of the proposed uncertainty analysis technique in two user trials. The proposed technique was able to detect unsafe decisions of the exoskeleton and tuned

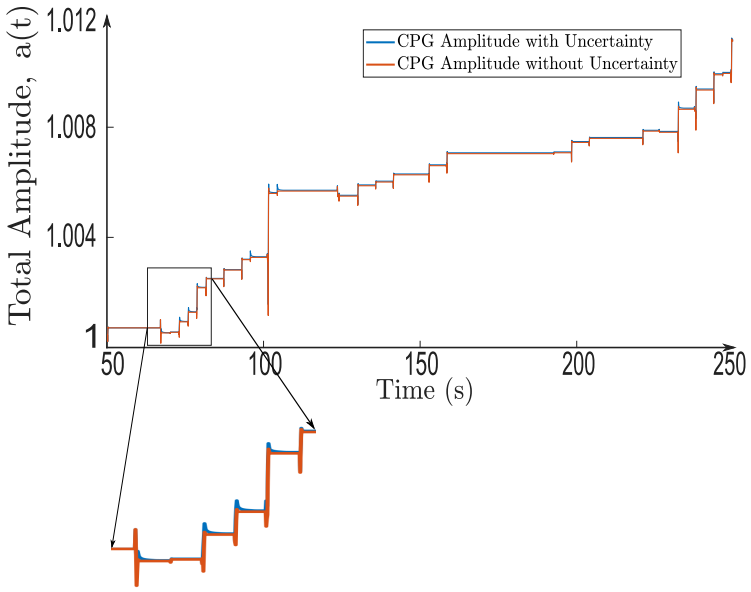

(a) Comparison of amplitude of the desired trajectory with and without uncertainty analysis.

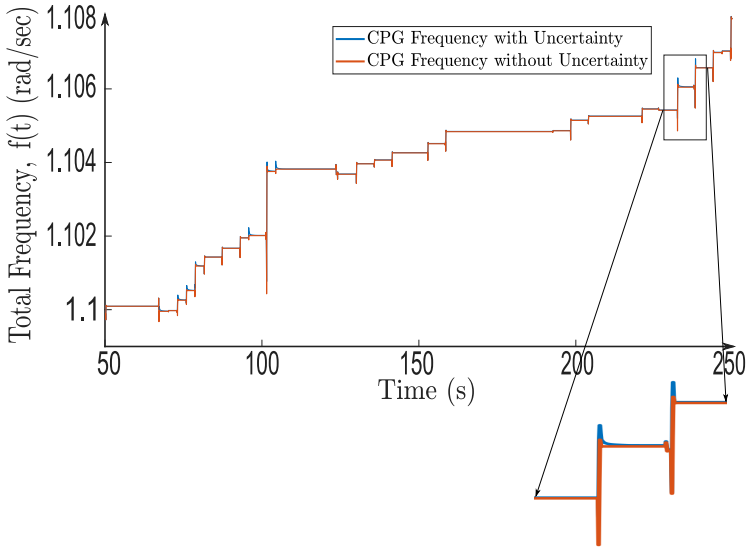

(b) Comparison of frequency of the desired trajectory with and without uncertainty analysis.

Figure 5.9: Performance of the proposed uncertainty analysis algorithm in adjusting trajectory's amplitude and frequency during user trial # 2.

CPGs gains considering the level of uncertainty in the coming data during both user trials.

Although the proposed method has the ability to reduce the safety concerns in using medical robots for clinical applications, it has some limitations that

need to be addressed. In the next steps of this project, we will address the concerns and limitations of the proposed method. The first concern is the energy loss in changing trajectories generated by CPGs. This issue has a direct impact on the ability of our proposed method to satisfy the preferences of the user. The second concern is fixing the user-dependant nature of the training data which can be fixed by state-of-the-art online learning algorithms like reinforcement learning. The last concern is the stability analysis of the gait generated by the CPGs which can be addressed in future. The proposed method can be used as a framework for uncertainty analysis and will be used in different medical robotic applications in the future.

Chapter 6

Conclusions and Future Directions

6.1 Conclusions

This thesis has presented research on the motion planning of robotic systems in diagnostic and therapy applications, with a focus on integrating control and AI techniques. Three main contributions have been discussed, each addressing important aspects of medical robotics. The first contribution introduced a novel robotic ultrasound imaging method, enabling precise scanning of the breast for high-quality ultrasound images. The second contribution presented a robot-assisted ultrasound scanning system designed to minimize the risk of COVID-19 transmission by automating tissue scanning with a dexterous robot arm. The system continuously assesses image quality and adjusts the probe contact force for better results. Finally, the third contribution centred around safety and uncertainty analysis in deep learning-based medical robotic applications, proposing a novel framework for uncertainty-aware control. By quantifying uncertainty levels and detecting out-of-distribution data, this framework ensures safe and reliable human-robot interactions. These advancements hold the potential for enhancing medical robotics' efficacy and safety, benefiting both patients and healthcare providers.

In chapter 3, we presented a method for defining a 5-DoF ultrasound (US) scanning trajectory based on the geometrical features of a target seroma within the breast. The proposed method employed a visual servoing algorithm to

update two controlled DoFs in real-time during scanning, ensuring adequate probe contact and improved visualization of the seroma in the US images. Referred to as the post-scan, our trajectory generation and visual servoing method relied on information gathered from a manual pre-scan set of images. During the pre-scan, images were captured at arbitrary orientations and positions, and the pose of the US probe was recorded. Geometrical information of the seroma inside the breast was extracted from the pre-scan images, approximating the seroma by an ellipsoid. The center and principal axes of the ellipsoid were utilized in defining the post-scan trajectory. For the post-scan, the desired trajectory of the US probe was calculated by intersecting a plane containing the ellipsoid's principal axis with the breast's surface, generating the $x - y - z$ trajectory points. The in-plane and out-of-plane rotation of the probe were determined at each point based on geometrical analysis of the seroma. The in-plane orientation of the probe was updated using an online segmentation algorithm that locates the center of the seroma and aligns the probe towards it. Additionally, the desired z position of the probe was updated using the average confidence map from the US image during scanning to ensure sufficient breast-probe contact. The proposed method was evaluated experimentally using plastisol phantoms, demonstrating its ability to orient the probe to keep the seroma centered in the acquired image while maintaining sufficient probe contact with minimal deformation.

Chapter 4 presented an algorithm for US image quality assessment that is utilized for robotic control of US scanning. Our proposed algorithm incorporates feature extraction and an SVM classifier to evaluate the quality of acquired images. By analyzing correlation, compression, and noise features, the algorithm estimates the quality of the US images, distinguishing between high-quality and low-quality ones. Integrated into the real-time control loop of the robotic US image scanning system, the algorithm allows the user to position the US probe at a specific location on the tissue, while the algorithm modulates the US scanning force applied to the tissue using an internal admittance controller. To validate the system's performance, we conducted evaluations using various quality assessment metrics, which demonstrated a

close correlation between manual subjective assessment of the captured US image quality and the quality estimation derived from our algorithm.

In chapter 5, we addressed the safety and security concerns of integrating deep learning into the control loop of medical robots, a safety-critical application. Our proposed method evaluates the uncertainty of the deep learning algorithm in real-time and utilizes this measure in the robot's control loop to ensure user safety. During the training phase, the method calculates the Kullback-Leibler (KL) divergence between predictions and labels to obtain the initial uncertainty of the model. Additionally, the method finds the distribution of predictions when the training features are fed into the model. The uncertainty of the prediction for a test feature is updated using the Mahalanobis distance from the training distribution. The calculated uncertainty influences the energy transfer between the user and the robot in the CPGs dynamics. We tested the proposed method on the ExoH3 exoskeleton with six degrees of freedom. Two scenarios were considered: the user walking with the exoskeleton and applying active torque to revise the CPG dynamics, and the evaluation of the uncertainty analysis technique in two user trials. The results demonstrate the ability of the proposed technique to detect unsafe decisions of the exoskeleton and adjust CPGs gains considering the level of uncertainty in the incoming data during both user trials.

6.2 Future Directions

For future research in the field of motion planning for ultrasound breast scanning surgery, there are several avenues to explore. One direction is the development of a robust 3D reconstruction algorithm that can automatically generate a detailed 3D volume of the breast using pre-scan images. This advancement would enhance the control of the robot during the visual servoing process, providing more accurate and precise localization of the seroma in the post-scan phase. By incorporating advanced 3D reconstruction techniques, the proposed method can further improve the overall efficiency and accuracy of the ultrasound breast scanning process.

Another aspect to consider for future research is the integration of needle insertion control into the system. The introduction of a new set of features that enables precise control of the ultrasound probe when a needle is inserted inside the breast would be highly beneficial. This feature would facilitate better visualization of both the seroma and the needle during scanning, ensuring safer and more efficient breast biopsy procedures. By incorporating needle insertion control, the proposed method can extend its capabilities to address a wider range of clinical applications, thus advancing the field of ultrasound-guided breast interventions.

For researchers interested in continuing this research, exploring full autonomy in controlling the orientation of the ultrasound probe is an exciting direction to pursue. Achieving six degrees of freedom during scanning would elevate the robotic system's capabilities, providing greater flexibility and adaptability in various scanning scenarios. Additionally, considering the integration of the quality assessment algorithm into a teleoperation system holds potential for remote-controlled ultrasound scanning robots. Such a system would empower medical professionals to perform ultrasound scans from a distance, making it particularly valuable in telemedicine and situations where in-person access is limited or unsafe.

For future researchers, we recommend further exploring and advancing the proposed method for rehabilitation motion planning with medical robots. The potential impact of this research is important, as it addresses safety concerns and limitations while enhancing the effectiveness of robotic rehabilitation in clinical applications. To build upon the current work, researchers should focus on the following key areas:

- Optimize Trajectory Generation: Investigate innovative techniques to optimize trajectory generation by Central Pattern Generators (CPGs) to reduce energy loss during motion planning. By minimizing energy consumption, the rehabilitation process can become more efficient and user-friendly, leading to improved patient experiences.

- Integrate Online Learning Algorithms: Overcome the user-dependent

nature of training data by incorporating state-of-the-art online learning algorithms, such as reinforcement learning. Adaptive learning methods will enable the proposed framework to continuously adapt to individual user preferences, providing a more personalized and effective rehabilitation experience.

- Conduct Stability Analysis: Perform thorough stability analysis of the gaits generated by CPGs to ensure the safety and reliability of the rehabilitation motion planning. Validating the stability of generated gaits is crucial for providing confidence in the robot's ability to support patients during their rehabilitation exercises without compromising safety.

- Explore Broad Applications: Extend the proposed uncertainty analysis framework to various medical robotic applications beyond rehabilitation. Investigating its integration in different clinical settings will enhance safety and reliability across diverse medical contexts, contributing to the advancement of medical robotics.

Embracing these recommendations will drive advancements in robotic-assisted rehabilitation, ultimately contributing to the improvement of healthcare practices and patient well-being.

References

[1] A. AbbasiMoshaii and F. Najafi, "Design, evaluation and prototyping of a new robotic mechanism for ultrasound imaging," *Journal of Computational Applied Mechanics*, vol. 50, no. 1, pp. 108–117, 2019.

[2] M. Abdar, F. Pourpanah, S. Hussain, *et al.*, "A review of uncertainty quantification in deep learning: Techniques, applications and challenges," *Information Fusion*, vol. 76, pp. 243–297, 2021.

[3] L. Abdel-Hamid, A. El-Rafei, S. El-Ramly, G. Michelson, and J. Hornegger, "Retinal image quality assessment based on image clarity and content," *Journal of biomedical optics*, vol. 21, no. 9, p. 096 007, 2016.

[4] M. Antico, F. Sasazawa, L. Wu, *et al.*, "Ultrasound guidance in minimally invasive robotic procedures," *Medical image analysis*, vol. 54, pp. 149–167, 2019.

[5] D. Berend, X. Xie, L. Ma, *et al.*, "Cats are not fish: Deep learning testing calls for out-of-distribution awareness," in *Proceedings of the 35th IEEE/ACM International Conference on Automated Software Engineering*, New York, NY, USA: Association for Computing Machinery, Dec. 2020, pp. 1041–1052.

[6] L. Bertoni, S. Kreiss, and A. Alahi, "Monoloco: Monocular 3d pedestrian localization and uncertainty estimation," in *Proceedings of the IEEE/CVF International Conference on Computer Vision*, 2019, pp. 6861–6871.

[7] N. Buda, E. Segura-Grau, J. Cylwik, and M. Wełnicki, "Lung ultrasound in the diagnosis of covid-19 infection-a case series and review of the literature," *Advances in medical sciences*, 2020.

[8] J. Carriere, J. Fong, T. Meyer, *et al.*, "An admittance-controlled robotic assistant for semi-autonomous breast ultrasound scanning," in *2019 International Symposium on Medical Robotics (ISMR)*, IEEE, 2019, pp. 1–7.

[9] P. Chatelain, A. Krupa, and N. Navab, "Optimization of ultrasound image quality via visual servoing," in *2015 IEEE international conference on robotics and automation (ICRA)*, IEEE, 2015, pp. 5997–6002.

[10] P. Chatelain, A. Krupa, and N. Navab, "Confidence-driven control of an ultrasound probe: Target-specific acoustic window optimization," in *2016 IEEE International Conference on Robotics and Automation (ICRA)*, IEEE, 2016, pp. 3441–3446.

[11] W. Chen, K. Gu, T. Zhao, G. Jiang, and P. Le Callet, "Semi-reference sonar image quality assessment based on task and visual perception," *IEEE Transactions on Multimedia*, 2020.

[12] L. S. Chow and R. Paramesran, "Review of medical image quality assessment," *Biomedical signal processing and control*, vol. 27, pp. 145–154, 2016.

[13] F. Dimeas and N. Aspragathos, "Online stability in human-robot cooperation with admittance control," *IEEE transactions on haptics*, vol. 9, no. 2, pp. 267–278, 2016.

[14] L.-A. Duflot, A. Krupa, B. Tamadazte, and N. Andreff, "Towards ultrasound-based visual servoing using shearlet coefficients," in *2016 IEEE International Conference on Robotics and Automation (ICRA)*, IEEE, 2016, pp. 3420–3425.

[15] T.-Y. Fang, H. K. Zhang, R. Finocchi, R. H. Taylor, and E. M. Boctor, "Force-assisted ultrasound imaging system through dual force sensing and admittance robot control," *International journal of computer assisted radiology and surgery*, vol. 12, no. 6, pp. 983–991, 2017.

[16] F. Ferraguti, C. Talignani Landi, L. Sabattini, M. Bonfè, C. Fantuzzi, and C. Secchi, "A variable admittance control strategy for stable physical human–robot interaction," *The International Journal of Robotics Research*, vol. 38, no. 6, pp. 747–765, 2019.

[17] J. Fong and M. Tavakoli, "Kinesthetic teaching of a therapist's behavior to a rehabilitation robot," in *2018 International Symposium on Medical Robotics (ISMR)*, IEEE, 2018, pp. 1–6.

[18] Y. Gal and Z. Ghahramani, "Dropout as a bayesian approximation: Representing model uncertainty in deep learning," in *international conference on machine learning*, PMLR, 2016, pp. 1050–1059.

[19] Y. Gal, J. Hron, and A. Kendall, "Concrete dropout," *arXiv preprint arXiv:1705.07832*, 2017.

[20] L. Grady, "Random walks for image segmentation," *IEEE transactions on pattern analysis and machine intelligence*, vol. 28, no. 11, pp. 1768–1783, 2006.

[21] K. Gui, H. Liu, and D. Zhang, "A generalized framework to achieve coordinated admittance control for multi-joint lower limb robotic exoskeleton," in *2017 International Conference on Rehabilitation Robotics (ICORR)*, IEEE, 2017, pp. 228–233.

[22] M. C. Hemmsen, M. M. Petersen, S. I. Nikolov, M. B. Nielsen, and J. A. Jensen, "Ultrasound image quality assessment: A framework for evaluation of clinical image quality," in *Medical Imaging 2010: Ultrasonic Imaging, Tomography, and Therapy*, International Society for Optics and Photonics, vol. 7629, 2010.

[23] D. Hendrycks and K. Gimpel, "A baseline for detecting misclassified and out-of-distribution examples in neural networks," *arXiv preprint arXiv:1610.02136*, 2016.

[24] D. Hendrycks, M. Mazeika, and T. Dietterich, "Deep anomaly detection with outlier exposure," *arXiv preprint arXiv:1812.04606*, 2018.

[25] P. Izmailov, S. Vikram, M. D. Hoffman, and A. G. G. Wilson, "What are bayesian neural network posteriors really like?" In *International conference on machine learning*, PMLR, 2021, pp. 4629–4640.

[26] C. I. Jarvis, K. Van Zandvoort, A. Gimma, *et al.*, "Quantifying the impact of physical distance measures on the transmission of covid-19 in the uk," *BMC medicine*, vol. 18, pp. 1–10, 2020.

[27] Y.-H. Jin, L. Cai, Z.-S. Cheng, *et al.*, "A rapid advice guideline for the diagnosis and treatment of 2019 novel coronavirus (2019-ncov) infected pneumonia (standard version)," *Military Medical Research*, 2020.

[28] A. Karamalis, W. Wein, T. Klein, and N. Navab, "Ultrasound confidence maps using random walks," *Medical image analysis*, vol. 16, no. 6, pp. 1101–1112, 2012.

[29] A. Q. Keemink, H. van der Kooij, and A. H. Stienen, "Admittance control for physical human–robot interaction," *The International Journal of Robotics Research*, vol. 37, no. 11, pp. 1421–1444, 2018.

[30] B. Lakshminarayanan, D. Tran, J. Liu, S. Padhy, T. Bedrax-Weiss, and Z. Lin, "Simple and principled uncertainty estimation with deterministic deep learning via distance awareness," 2020.

[31] C. T. Landi, F. Ferraguti, L. Sabattini, C. Secchi, and C. Fantuzzi, "Admittance control parameter adaptation for physical human-robot interaction," in *2017 IEEE international conference on robotics and automation (ICRA)*, IEEE, 2017, pp. 2911–2916.

[32] K. Lee, K. Lee, H. Lee, and J. Shin, "A simple unified framework for detecting out-of-distribution samples and adversarial attacks," *Advances in neural information processing systems*, vol. 31, 2018.

[33] Z. Li, B. Huang, Z. Ye, M. Deng, and C. Yang, "Physical human–robot interaction of a robotic exoskeleton by admittance control," *IEEE Transactions on Industrial Electronics*, vol. 65, no. 12, pp. 9614–9624, 2018.

[34] S. Liang, Y. Li, and R. Srikant, "Enhancing the reliability of out-of-distribution image detection in neural networks," *arXiv preprint arXiv:1706.02690*, 2017.

[35] J. S. Lim, "Two-dimensional signal and image processing," 1990.

[36] J. Liu, Z. Lin, S. Padhy, D. Tran, T. Bedrax Weiss, and B. Lakshminarayanan, "Simple and principled uncertainty estimation with deterministic deep learning via distance awareness," *Advances in Neural Information Processing Systems*, vol. 33, pp. 7498–7512, 2020.

[37] E. Marchand, "Subspace-based direct visual servoing," *IEEE Robotics and Automation Letters*, vol. 4, no. 3, pp. 2699–2706, 2019.

[38] C. McDermott, J. Daly, and S. Carley, "Combatting covid-19: Is ultrasound an important piece in the diagnostic puzzle?" *Emergency Medicine Journal*, vol. 37, no. 10, pp. 644–649, 2020.

[39] J. K. Mehr, M. Sharifi, V. K. Mushahwar, and M. Tavakoli, "Intelligent locomotion planning with enhanced postural stability for lower-limb exoskeletons," *IEEE Robotics and Automation Letters*, vol. 6, no. 4, pp. 7588–7595, 2021.

[40] L. Morawska and D. K. Milton, "It is time to address airborne transmission of covid-19," *Clinical Infection Diseases*, vol. 6, p. 939, 2020.

[41] A. A. Moshaii and F. Najafi, "A review of robotic mechanisms for ultrasound examinations," *Industrial Robot: An International Journal*, 2014.

[42] Z. Nado, N. Band, M. Collier, *et al.*, "Uncertainty baselines: Benchmarks for uncertainty & robustness in deep learning," *arXiv preprint arXiv:2106.04015*, 2021.

[43] F. Najafi and N. Sepehri, "A robotic wrist for remote ultrasound imaging," *Mechanism and machine theory*, vol. 46, no. 8, pp. 1153–1170, 2011.

[44] M. Ng, "Estimating uncertainty in neural networks for cardiac mri segmentation," Ph.D. dissertation, University of Toronto (Canada), 2020.

[45] M. Ng, F. Guo, L. Biswas, *et al.*, "Estimating uncertainty in neural networks for cardiac mri segmentation: A benchmark study," *arXiv preprint arXiv:2012.15772*, 2020.

[46] NHL, "Ultrasound scanning," https://www.nhs.uk/conditions/ultrasound-scan Last accessed: 25 May 2018, 2018.

[47] S. O'Sullivan, N. Nevejans, C. Allen, *et al.*, "Legal, regulatory, and ethical frameworks for development of standards in artificial intelligence (ai) and autonomous robotic surgery," *The international journal of medical robotics and computer assisted surgery*, vol. 15, no. 1, e1968, 2019.

[48] M. Ourak, B. Tamadazte, O. Lehmann, and N. Andreff, "Direct visual servoing using wavelet coefficients," *IEEE/ASME Transactions on Mechatronics*, vol. 24, no. 3, pp. 1129–1140, 2019.

[49] F. Pedregosa, G. Varoquaux, A. Gramfort, *et al.*, "Scikit-learn: Machine learning in Python," *Journal of Machine Learning Research*, vol. 12, pp. 2825–2830, 2011.

[50] J. Piwowarczyk, J. Carriere, K. Adams, and M. Tavakoli, "An admittance-controlled force-scaling dexterous assistive robotic system," in *2020 Journal of Medical Robotics Research (JMRR)*, 2020, pp. 1–16.

[51] J. R. Quinlan, "Induction of decision trees," *Machine learning*, vol. 1, no. 1, pp. 81–106, 1986.

[52] G. P. Renieblas, A. T. Nogués, A. M. González, N. G. León, and E. G. Del Castillo, "Structural similarity index family for image quality assessment in radiological images," *Journal of medical imaging*, vol. 4, no. 3, p. 035 501, 2017.

[53] S. R. Safavian and D. Landgrebe, "A survey of decision tree classifier methodology," *IEEE transactions on systems, man, and cybernetics*, vol. 21, no. 3, pp. 660–674, 1991.

[54] E. Sartori, C. Tadiello, C. Secchi, and R. Muradore, "Tele-echography using a two-layer teleoperation algorithm with energy scaling," in *2019 International Conference on Robotics and Automation (ICRA)*, IEEE, 2019, pp. 1569–1575.

[55] L. Schinaia, A. Scorza, F. Orsini, and S. Sciuto, "Feature classification in ultrasound textures for image quality assessment: A preliminary study on the characterization and selection of haralick parameters by means of correlation matrices," in *22nd IMEKO TC4 International Symposium & 20th International Workshop on ADC Modelling and Testing Supporting World Development through Electrical&Electronic Measurements*, 2017, pp. 170–174.

[56] S. O. Schrade, Y. Nager, A. R. Wu, R. Gassert, and A. Ijspeert, "Bio-inspired control of joint torque and knee stiffness in a robotic lower limb exoskeleton using a central pattern generator," in *2017 International Conference on Rehabilitation Robotics (ICORR)*, IEEE, 2017, pp. 1387–1394.

[57] J. Schwaab, Y. Diez, A. Oliver, *et al.*, "Automated quality assessment in three-dimensional breast ultrasound images," *Journal of Medical Imaging*, vol. 3, no. 2, p. 027 002, 2016.

[58] J. Serrà, D. Álvarez, V. Gómez, O. Slizovskaia, J. F. Núñez, and J. Luque, "Input complexity and out-of-distribution detection with likelihood-based generative models," *arXiv preprint arXiv:1909.11480*, 2019.

[59] M. Sharifi, J. K. Mehr, V. K. Mushahwar, and M. Tavakoli, "Adaptive cpg-based gait planning with learning-based torque estimation and control for exoskeletons," *IEEE Robotics and Automation Letters*, vol. 6, no. 4, pp. 8261–8268, 2021.

[60] M. Sharifi, J. K. Mehr, V. K. Mushahwar, and M. Tavakoli, "Autonomous locomotion trajectory shaping and nonlinear control for lower limb exoskeletons," *IEEE/ASME Transactions on Mechatronics*, vol. 27, no. 2, pp. 645–655, 2022.

[61] M. Sharifi, H. Salarieh, S. Behzadipour, and M. Tavakoli, "Tele-echography of moving organs using an impedance-controlled telerobotic system," *Mechatronics*, vol. 45, pp. 60–70, 2017.

[62] M. Tavakoli, J. Carriere, and A. Torabi, "Robotics, smart wearable technologies, and autonomous intelligent systems for healthcare during the covid-19 pandemic: An analysis of the state of the art and future vision," *Advanced Intelligent Systems*, p. 2 000 071, 2020.

[63] Z. Wang, A. C. Bovik, H. R. Sheikh, and E. P. Simoncelli, "Image quality assessment: From error visibility to structural similarity," *IEEE transactions on image processing*, vol. 13, no. 4, pp. 600–612, 2004.

[64] M. Welleweerd, A. de Groot, S. de Looijer, F. Siepel, and S. Stramigioli, "Automated robotic breast ultrasound acquisition using ultrasound feedback," in *2020 IEEE International Conference on Robotics and Automation (ICRA)*, IEEE, 2020, pp. 9946–9952.

[65] Y. Wen, P. Vicol, J. Ba, D. Tran, and R. Grosse, "Flipout: Efficient Pseudo-Independent weight perturbations on Mini-Batches," Mar. 2018. arXiv: `1803.04386 [cs.LG]`.

[66] L. Wu, J.-Z. Cheng, S. Li, B. Lei, T. Wang, and D. Ni, "FUIQA: Fetal ultrasound image quality assessment with deep convolutional networks," *IEEE transactions on cybernetics*, vol. 47, no. 5, pp. 1336–1349, 2017.

[67] C. Yang, G. Peng, Y. Li, R. Cui, L. Cheng, and Z. Li, "Neural networks enhanced adaptive admittance control of optimized robot–environment interaction," *IEEE transactions on cybernetics*, vol. 49, no. 7, pp. 2568–2579, 2018.

[68] R. J. Zemp, C. K. Abbey, and M. F. Insana, "Generalized neq for assessment of ultrasound image quality," in *Medical Imaging 2003: Physics of Medical Imaging*, International Society for Optics and Photonics, vol. 5030, 2003, pp. 391–402.

[69] G. Zeng and A. Hemami, "An overview of robot force control," *Robotica*, vol. 15, no. 5, pp. 473–482, 1997.

[70] D. Zhang, Y. Ren, K. Gui, J. Jia, and W. Xu, "Cooperative control for a hybrid rehabilitation system combining functional electrical stimulation and robotic exoskeleton," *Frontiers in neuroscience*, vol. 11, p. 725, 2017.

[71] L. Zhang, N. J. Dudley, T. Lambrou, N. Allinson, and X. Ye, "Automatic image quality assessment and measurement of fetal head in two-dimensional ultrasound image," *Journal of Medical Imaging*, vol. 4, no. 2, p. 024 001, 2017.

[72] X. Zhang, X. Xie, L. Ma, *et al.*, "Towards characterizing adversarial defects of deep learning software from the lens of uncertainty," in *Proceedings of the ACM/IEEE 42nd International Conference on Software Engineering*, ser. ICSE '20, Seoul, South Korea: Association for Computing Machinery, Jun. 2020, pp. 739–751.

[73] Z. Y. Zu, M. D. Jiang, P. P. Xu, *et al.*, "Coronavirus disease 2019 (covid-19): A perspective from china," *Radiology*, p. 200 490, 2020.

Appendix A

Appendix: List of Variables and Distribution Analysis

A.1 List of Variables and Definitions

- τ_{input} Total Torque Measured by Torque Sensors
- τ_{exo} HRI Torque Applied to Exoskeleton's Joints
- τ_{motor} Exoskeleton Motor Torque
- τ_h Human Torque Vector
- τ_{HRI} Physical Human-robot Interaction Torque
- $\tau_{h,pass}$ Passive Torque Dynamic of Human-Exoskeleton
- $M_q(q)$ Inertia Matrix
- $C_q(q)$ Coriolis, Centrifugal and Damping Term
- $G_q(q)$ Gravitational Torque
- $q, \dot{q}, \ddot{q}$ Position, Velocity and Acceleration of Joints
- $E_i(t)$ Energy Transferred to Joint i
- N_i Number of Adjacent Joints to Joint i
- $a(t)$ Amplitude of the Movement

- $f(t)$ Frequency of the Movement
- f_{test} Test Feature
- $C_{RF}(f_{test})$ Adaptable Uncertainty Gain
- D Adaptable Uncertainty Threshold
- c_{i_j}, d_{i_j} Fourier Series Coefficients
- O_{train} Random Forest Predictions for Training Data
- L_{train} Training Labels
- F_{train} Training Features
- D_{KL} KL Divergence
- D_M Mahalanobis Distance
- D_{M_t} Mahalanobis Distance after Thresholding
- $P_l(\overrightarrow{x})$ Distribution of Training Labels
- $P_p(\overrightarrow{x})$ Distribution of Training Predictions
- $P_t(\overrightarrow{x})$ Distribution of Training Set
- $\overrightarrow{x}$ Vector of One Feature
- x_i Element of Feature Vector
- y_i Sample from Training Predictions
- N_f Total Number of Samples in Feature Set
- μ_l, σ_l Training Labels Mean and Standard Deviation
- μ_p, σ_p Predictions Mean and Standard Deviation
- μ_f, Σ_f Training Data Mean and Standard Deviation

A.2 Distribution Analysis

Let us define x_i as a sample from $\overrightarrow{x}$, where $\overrightarrow{x}$ is the vector of one feature and x_i is an element of this vector ($x_i \in \overrightarrow{x}$). Then n_{x_i} is the number of times that the input data is in the interval of $[x_i - \epsilon, x_i + \epsilon]$. Here ϵ is the value that controls the length of histogram intervals in our probability function estimation. Then we have

$$\begin{aligned} \sum_{i=1}^{M} n_{x_i} &= N_f \\ P_{x_i} &= \frac{n_{x_i}}{N_f}. \end{aligned} \tag{A.1}$$

Here, M is the number of distinguished samples and N_f is the total number of samples in the dataset. We need to calculate the distribution of the dataset to find KL divergence using (5.6), while (A.1) is only useful for finding the probability of one sample. To solve this problem, we estimate the distribution of (L_{train}) and (O_{train}) using Gaussian fitting as the distribution of the acquired data follows Gaussian distribution shown in Figure A.1. Then we have

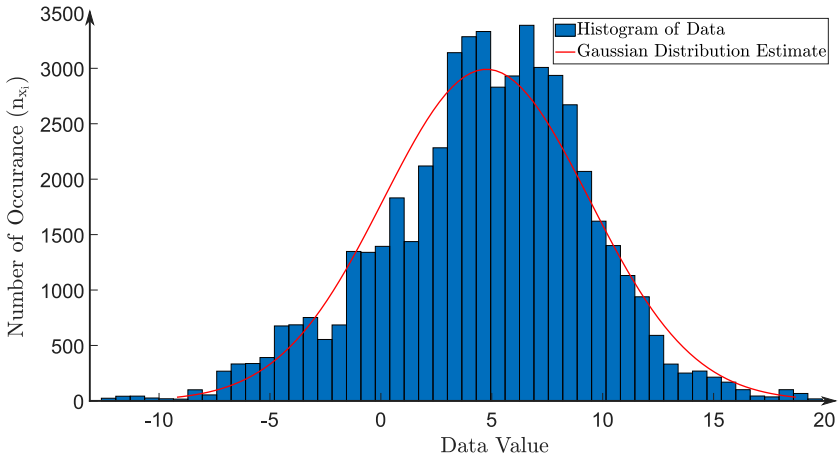

Figure A.1: Training dataset with Gaussian distribution fitted to the data.

$$L_{train} \sim \mathcal{N}(\mu_l, \sigma_l), \tag{A.2}$$

where mean value (μ_l) and standard deviation (σ_l) can be calculated using $\mu_l = \sum_{i=1}^{N} x_i$ and $\sigma_l = \sqrt{\frac{1}{N}\sum_{i=1}^{N}(x_i - \mu_l)^2}$. We now formalize the distribution of the training labels $P_l(\overrightarrow{x})$ as

$$P_l(\overrightarrow{x}) = \frac{1}{\sqrt{2\pi\sigma_l^2}} \exp \frac{(\overrightarrow{x} - \overrightarrow{\mu_l})^2}{2\sigma_l^2}. \tag{A.3}$$

We follow the same procedure for finding the distributions of O_{trains} ($P_p(\overrightarrow{x})$) as

$$\begin{aligned} O_{train} &\sim \mathcal{N}(\mu_p, \sigma_p) \\ \mu_p &= \sum_{i=1}^{N} y_i \\ \sigma_p &= \sqrt{\frac{1}{N}\sum_{i=1}^{N}(y_i - \mu_p)^2}. \end{aligned} \tag{A.4}$$

We now formalize $P_p(\overrightarrow{x})$ as

$$P_p(\overrightarrow{y}) = \frac{1}{\sqrt{2\pi\sigma_p^2}} \exp \frac{(\overrightarrow{y} - \overrightarrow{\mu_p})^2}{2\sigma_p^2}. \tag{A.5}$$

Here, y_i is the sample from O_{train}. We calculate the required distributions using (A.3) and (A.5), then we use (5.6) for calculating KL divergence between distributions as our initial uncertainty measure.